Experimental investigation on the validity of the local thermal equilibrium assumption in ablative-material response models

Shaolin Liu, Azita Ahmadi-Senichault, Cyril Levet, Jean Lachaud

Experimental investigation on the validity of the local thermal equilibrium assumption in ablative-material response models

Shaolin Liu[a,b,*], Azita Ahmadi-Senichault[a,b], Cyril Levet[a,b] and Jean Lachaud[b,c]

[a]Arts et Métiers Institute of Technology, 33400, Talence, France
[b]I2M - Institute of Mechanical Engineering of Bordeaux: UMR CNRS 5295, University of Bordeaux, Arts et Métiers Institute of Technology, Hesam Université, Bordeaux INP, INRAE, 33400, Talence, France
[c]Univ. Bordeaux, 33400, Talence, France

ARTICLE INFO

Keywords:
Local thermal non-equilibrium
Anisotropic porous materials
Macroscopic numerical simulations
Heat exchange coefficient
Experimental study
Inverse method

ABSTRACT

Thermal Protection Systems (TPS) material response models rely on the assumption of local thermal equilibrium (LTE) between the solid phase and the gas phase. This assumption was challenged and investigated by several authors but a sufficiently precise knowledge of heat transfer coefficients in TPS materials was lacking to reach final conclusions. The objective of this work is to contribute to filling this gap by performing an experimental/numerical analysis of this assumption for Calcarb, a commercial carbon preform used for manufacturing thermal protection systems. Heat transfer within Calcarb was studied experimentally in the Through-Thickness (TT) and in the In-Plane (IP) directions for Reynolds numbers of 1 to 4 - representative of the TPS application - using the transient single-blow technique (TSBT). Numerical parameter estimation was performed using the Porous material Analysis Toolbox based on OpenFoam (PATO) and the Design Analysis Kit for Optimization and Terascale Applications (DAKOTA). The heat transfer coefficient h_v is found to be greater than or equal to 10^8 W/(m^3 · K) and the LTE assumption is shown to be valid in the conditions of the experiment. To assess the validity of the LTE assumption for other conditions, the above bound of h_v may now be used in combination with a local thermal non-equilibrium model.

1. Introduction

Carbon fiber felts are widely used in the industry as insulators in high-temperature furnaces. At the end of the 1990s, NASA used a rigid carbon felt called FiberForm, produced by Fiber Materials Inc., to develop a new generation of low-density ablative materials to protect space vehicles during hypersonic atmospheric entry [1]. This new class of ablative materials called Phenolic Impregnated Carbon Ablators (PICA) has flawlessly been used since then: Stardust (NASA, 2006) [2, 3], Mars Science Laboratory (NASA, 2012) [4, 5], Mars 2020 (NASA, 2021) [6, 7], Dragon vehicles (SpaceX, since 2012) [8]. The European Space Agency and ArianeGroup have developed ASTERM [9] based on Calcarb, produced by Mersen. FiberForm and Calcarb are both made of chopped carbon fibers of millimeter length and of about 10 micrometers in diameter [1, 10, 11] as shown in Fig.1. During the manufacturing process, the carbon fibers tend to align according to the compression plane resulting in anisotropic properties. The direction perpendicular to this plane is referred to as "Through-Thickness" (TT) and that parallel as "In-Plane" (IP); they are shown in Fig.2. The thermal conductivity ratio between IP and TT directions is of about two [12]. When possible, the anisotropy is used to optimize the design of thermal protection systems (TPS) by placing the TT direction perpendicular to the vehicle's surface. This obviously helps reducing heat transfer towards the internal structure but it is also helpful in diffusing heat away from hot spots (stagnation point, shoulders) thanks to the higher IP-direction conductivity. Additionally, carbon preforms are impregnated with a low-density phenolic polymer to improve thermal protection by reducing internal radiation, by acting as a heat sink through endothermic pyrolysis processes, and by blowing pyrolysis gases in the boundary layer that partially block the incoming heat flux [13]. The velocity of the pyrolysis gases is of the order of 1 m/s at peak heating [5]. Detailed TPS material response models, taking into account this complex physics, have been developed since the 1950s, with strong progress in the 1960s during the design of the Apollo heat shield [14, 15]. They are currently being improved and adapted to new generations of materials by an active community [16] with the goal of reducing design

*Corresponding author at: Arts et Métiers Institute of Technology, 33400, Talence, France.
E-mail address: shaolin.liu@u-bordeaux.fr (S. Liu).

uncertainties [17, 18]. The generalization of the use of porous fibrous materials raises new questions regarding the validity of the inherited hypotheses, such as

Nomenclature

Greek symbols

ε_i volume fraction of the i-phase

μ_g dynamic viscosity of gas, kg m^{-1} s^{-1}

ρ_i density of the i-phase, kg m^{-3}

Latin symbols

A_{sg} area of the s-g interface contained in the averaging volume, V, m^2

$\mathbf{b_i}$ vector field that maps $\nabla \langle T_i \rangle^i$ onto $\tilde{T}_i$ in LTE model, $\tilde{T}_i = \mathbf{b_i} \cdot \nabla \langle T_i \rangle^i$

$\mathbf{b_{ii}}$ vector field that maps $\nabla \langle T_i \rangle^i$ onto $\tilde{T}_i$ in LTNE model

$c1 - c4$ coefficients associated with thermal conductivity

$c5, c6$ coefficients associated with thermal conductivity, W m^{-1} K^{-1}

$c_{p,i}$ heat capacity of the i-phase, J kg^{-1} K^{-1}

d_{cl} cluster fiber diameter, m

d_f fiber diameter, m

d_{par} particle diameter, m

d_p pore diameter, m

D tube diameter, m

h_s interstitial heat transfer coefficient, W m^{-2} K^{-1}

h_v volumetric heat transfer coefficient, W m^{-3} K^{-1}

H tube radius, m

$\mathbf{I}$ Identity tensor

k_t thermocouple or tube thermal conductivity, W m^{-1} K^{-1}

k_i thermal conductivity of the i-phase, W m^{-1} K^{-1}

$\mathbf{k_{i,eff}}$ effective thermal conductivity tensor of the i-phase, W m^{-1} K^{-1}

$\mathbf{K}$ permeability tensor, m^2

$\mathbf{k_{eff}}$ effective thermal conductivity tensor, W m^{-1} K^{-1}

$\mathbf{k_{dis}}$ dispersion term of the thermal conductivity, W m^{-1} K^{-1}

$\mathbf{k_{tor}}$ tortuosity term of the thermal conductivity, W m^{-1} K^{-1}

l_g the size of the unit cell, m

L sample length, m

M gas molar mass, kg mol^{-1}

$\mathbf{n_{gs}}$ outwardly directed unit normal vector pointing from the gas phase toward the solid phase, $\mathbf{n_{gs}} = -\mathbf{n_{sg}}$

Nu_s Nusselt number based on h_s

Nu_v Nusselt number based on h_v

p gas pressure, kg m^{-1} s^{-2}

$\langle p \rangle^g$ Intrinsic average pressure, kg m^{-1} s^{-2}

Pe Peclet number

Pr Prandtl number

qm gas mass-flow rate, kg s^{-1}

Q volumetric flow rate, m^3 s^{-1}

R gas constant, J K^{-1} mol^{-1}

Re_d Reynolds number based on the pore diameter

s_i scalar field used in LTNE model

T_i point temperature in the i-phase, K

$\langle T_i \rangle^i$ initrinsic phase average temperature in the i-phase, K

$\tilde{T}_i$ the spatial deviation temperature in the i-phase, $\tilde{T}_i = T_i - \langle T_i \rangle^i$, K

$\langle T \rangle$ spatial average temperature in the LTE model, K

$\mathbf{u}$ Darcy velocity, $\varepsilon_g \langle \mathbf{v_g} \rangle^{\mathbf{g}}$, m s^{-1}

u magnitude of the Darcy velocity, m s^{-1}

$\mathbf{v_g}$ velocity of the gas phase, m s^{-1}

$\langle \mathbf{v_g} \rangle^{\mathbf{g}}$ intrinsic phase average velocity of the gas, m s^{-1}

$\langle \mathbf{v_g} \rangle$ superficial average velocity, m s^{-1}

$\tilde{\mathbf{v}}_\mathbf{g}$ the deviation of gas velocity, $\tilde{\mathbf{v}}_\mathbf{g} = \mathbf{v_g} - \langle \mathbf{v_g} \rangle^{\mathbf{g}}$, m s^{-1}

V averaging volume, m^3

Subscripts

dis	dispersion
g	gas
in	inlet
m	mixture of gas and solid phases
num	numerical result
out	outlet
s	solid
t	thermocouple or tube
tor	tortuosity

the assumption of local thermal equilibrium ubiquitously used in TPS design. Heat transfer in porous materials can either be studied under the assumption of local thermal equilibrium (LTE) [19, 20] or local thermal non-equilibrium (LTNE) [21–25]. In LTE models, it is assumed that the average temperatures of the solid and gas phases are equal. Florio [26] and Puiroux [27, 28] demonstrated the validity of the local thermal equilibrium assumption for dense charring materials. However, Scoggins et al. [29] showed that the local thermal equilibrium assumption was invalid for PICA using available literature correlations to estimate the heat transfer coefficient between the solid phase and the gas flowing through the pores [29]. Unfortunately, correlations for materials similar to PICA were not available in the literature and the major recommendation of Scoggins et al. [29] was to perform experiments to measure the heat transfer coefficient in low-density carbon fiber materials. As such studies are still unavailable, the objective of this work is to contribute to filling this gap by investigating experimentally convective heat transfer in Calcarb. The problem is however more complex than it appears because the flow of gas through porous media also modifies their effective thermal conductivity through a process known as dispersion [30].

To introduce the studied problem, let us start by presenting a generic model that was proposed for porous reactive materials submitted to high temperatures under the assumption of local thermal equilibrium. This model implements the physics encountered in materials submitted to very high temperatures in different applications such as thermal protection systems of space vehicles, porous materials submitted to fire, or biomass in thermochemical processes of biofuel production [19]. For the purpose of this work we may ignore pyrolysis and chemistry terms and the mass and energy conservation equations write

$$\begin{cases} \frac{\partial}{\partial t}\left(\varepsilon_g \frac{M\langle p\rangle^g}{R\langle T\rangle}\right) + \nabla\cdot\left(-\frac{M\langle p\rangle^g}{R\langle T\rangle}\frac{\mathbf{K}}{\mu_g}\cdot\nabla\langle p\rangle^g\right) = 0 \\ \left(\varepsilon_g\rho_g c_{p,g} + \varepsilon_s\rho_s c_{p,s}\right)\frac{\partial\langle T\rangle}{\partial t} + \left(\varepsilon_g\rho_g c_{p,g} + \varepsilon_s\rho_s c_{p,s}\right)\langle\mathbf{v_g}\rangle^{\mathbf{g}}\cdot\nabla\langle T\rangle \\ = \nabla\cdot(\mathbf{k_{eff}}\cdot\nabla\langle T\rangle) \end{cases} \tag{1}$$

where the first equation is the gas mass conservation written in terms of gas pressure (the gas velocity is substituted with Darcy's law) and the second equation is the energy conservation. The gas volume fraction ε_g is equal to the porosity of the porous medium. $\mathbf{K}$ and $\mathbf{k_{eff}}$ denote the permeability and effective thermal conductivity tensors respectively. $\langle p\rangle^g$ and $\langle\mathbf{v_g}\rangle^g$ are the intrinsic average pressure and velocity of the gas. $\langle T\rangle$ denotes the superficial average temperature of the porous material (that is equal for both phases). The superficial and intrinsic phase averages of any quantity φ_i associated to the i-phase are respectively given by $\langle\varphi_i\rangle = \frac{1}{V}\int_{V_i}\varphi_i dV$, $\langle\varphi_i\rangle^i = \varepsilon_i^{-1}\langle\varphi_i\rangle = \frac{1}{V_i}\int_{V_i}\varphi_i dV$. In these relationships, V_i is the volume of the i-phase contained within the averaging volume V which is a representative elementary volume of the porous medium.

In Eq.1, the permeability $\mathbf{K}$ can be determined by experimental measurements or numerical simulations [31]. The effective conductivity, $\mathbf{k_{eff}}$, is known to be bounded by the arithmetic ($\mathbf{k_{eff}} = (\varepsilon_g k_g + \varepsilon_s k_s)\mathbf{I}$) and the harmonic ($\mathbf{k_{eff}} = (\varepsilon_s/k_s + \varepsilon_g/k_g)^{-1}\mathbf{I}$) averages of the solid and gas conductivities. Correlations for granular porous materials have been proposed in the literature [32–34], amongst which the most simple and often used one that reads $\mathbf{k_{eff}} = {k_g}^{\varepsilon_g}{k_s}^{\varepsilon_s}\mathbf{I}$ corresponds to the geometric average. In these equations, $\mathbf{k_{eff}}$ is treated as a spherical tensor and the effect of the gas flow on the effective thermal conductivity is not captured.

A theoretical expression of $\mathbf{k_{eff}}$ was later derived using upscaling techniques such as the volume-averaging method [30, 35–37]. As shown in Eq.2, besides the arithmetic average, two additional terms are involved: the tortuosity term that accounts for the microstructure of the material and the dispersion term that accounts for gas flow effects. These two terms may be numerically estimated by solving a closure problem on a periodic unit cell representative of the structure [35, 36, 38, 39].

$$\mathbf{k_{eff}} = \left(\varepsilon_g k_g + \varepsilon_s k_s\right)\mathbf{I} + \frac{k_g - k_s}{V}\int_{A_{gs}}\mathbf{n}_{gs}\mathbf{b}_g dA - \left(\rho c_p\right)_g\left\langle\tilde{\mathbf{v}}_g\mathbf{b}_g\right\rangle \tag{2}$$

where $\mathbf{v}_g$, $\langle\mathbf{v_g}\rangle^{\mathbf{g}}$, and $\tilde{\mathbf{v}}_g = \mathbf{v}_g - \langle\mathbf{v_g}\rangle^g$ are respectively the gas velocity within the pores, the intrinsic phase average velocity, and the deviation velocity. The closure variable $\mathbf{b}_g$ is the vector field that maps $\nabla\langle T_g\rangle^g$ onto $\tilde{T}_g$ in the LTE model, $\tilde{T}_g = \mathbf{b_g}\cdot\nabla\langle T_g\rangle^g$ and the LTE condition is represented by $\langle T\rangle = \langle T_g\rangle^g = \langle T_s\rangle^s$.

The generic LTE model needs to be upgraded when local thermal equilibrium is no longer valid, as explained in the previous paragraph. The mass and energy conservation equations

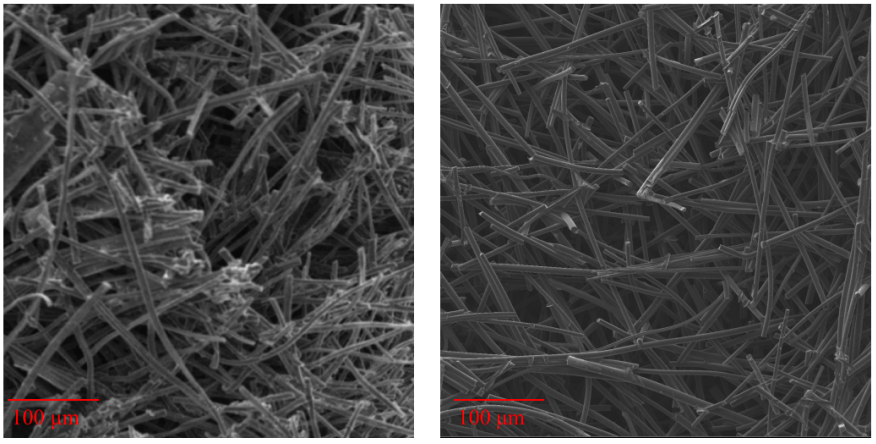

Figure 1: Scanning electron micrography (SEM) images of FiberForm (left) and Calcarb (right)

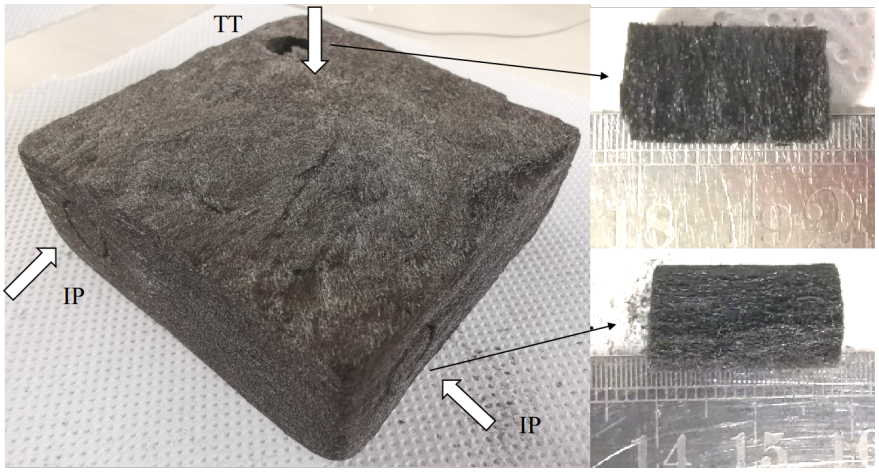

Figure 2: "Through-Thickness" (TT) and "In-Plane" (IP) directions in Calcarb

for the LTNE model in their simplest form [35] in the case of compressible and non reacting flows write

$$\begin{cases} \frac{\partial}{\partial t}\left(\varepsilon_g \frac{M\langle p\rangle^g}{R\langle T_g\rangle^g}\right) + \nabla\cdot\left(-\frac{M\langle p\rangle^g}{R\langle T_g\rangle^g}\frac{\mathbf{K}}{\mu_g}\cdot\nabla\langle p\rangle^g\right) = 0 \\ \frac{\partial}{\partial t}\left(\varepsilon_s\rho_s c_{p,s}\langle T_s\rangle^s\right) = \nabla\cdot(\mathbf{k_{s,eff}}\cdot\nabla\langle T_s\rangle^s) + h_v\left(\langle T_g\rangle^g - \langle T_s\rangle^s\right) \\ \frac{\partial}{\partial t}\left(\varepsilon_g\rho_g c_{p,g}\langle T_g\rangle^g\right) + \nabla\cdot(\rho_g c_{p,g}\langle \mathbf{v_g}\rangle^{\mathbf{g}}\langle T_g\rangle^g) \\ = \nabla\cdot(\mathbf{k_{g,eff}}\cdot\nabla\langle T_g\rangle^g) + h_v\left(\langle T_s\rangle^s - \langle T_g\rangle^g\right) \end{cases} \tag{3}$$

where $c_{p,i}$ and $\mathbf{k_{i,eff}}$ respectively denote the heat capacity and effective thermal conductivity tensor of the i phase. $\langle T_i\rangle^i$ and $\langle \mathbf{v_g}\rangle^{\mathbf{g}}$ denote the intrinsic phase average temperature for the i-phase and the intrinsic gas average velocity. h_v denotes the volumetric heat transfer coefficient between the gas stream and the sample. There are three effective properties, h_v, $\mathbf{k_{s,eff}}$ and $\mathbf{k_{g,eff}}$ to be determined. In many research works, regardless of the experimental conditions, simple expressions of $\mathbf{k_{s,eff}}$ and $\mathbf{k_{g,eff}}$ as a function of gas and solid phase conductivities and the porosity of the homogeneous and isotropic porous medium (metal foams, ceramic foams) have been considered [32, 34, 40–42]. $\mathbf{k_{i,eff}}$ are treated as scalars and are given by

$$\mathbf{k_{s,eff}} = \varepsilon_s k_s \mathbf{I} \qquad \mathbf{k_{g,eff}} = \varepsilon_g k_g \mathbf{I} \tag{4}$$

A more detailed formulation of $\mathbf{k_{s,eff}}$, $\mathbf{k_{g,eff}}$ and h_v in the LTNE model obtained by the volume-averaging method are given as follows [30, 35, 43],

$$\begin{cases} \mathbf{k_{s,eff}} = \varepsilon_s k_s \mathbf{I} + \frac{k_s}{V}\int_{A_{gs}} \mathbf{n}_{sg}\mathbf{b_{ss}}dA \\ \mathbf{k_{g,eff}} = \varepsilon_g k_g \mathbf{I} + \frac{k_g}{V}\int_{A_{gs}} \mathbf{n}_{gs}\mathbf{b_{gg}}dA - \rho_g c_{p,g}\left\langle \tilde{\mathbf{v}}_g \mathbf{b_{gg}}\right\rangle \\ h_v = \frac{k_g}{V}\int_{A_{gs}} \mathbf{n}_{gs}\nabla s_g dA \end{cases} \tag{5}$$

where the closure variables $\mathbf{b_{ii}}$, and s_i are the vector and scalar fields that maps $\nabla\langle T_i\rangle^i$ onto $\tilde{T}_i$ in the LTNE model, $\tilde{T}_g = \mathbf{b_{gg}}\cdot\nabla\langle T_g\rangle^g - s_g(\langle T_g\rangle^g - \langle T_s\rangle^s) + ...$, and $\tilde{T}_s = \mathbf{b_{ss}}\cdot\nabla\langle T_s\rangle^s -$

$s_s(\langle T_s\rangle^s - \langle T_g\rangle^g) + ...$ [35]. Compared to Eq.2, Eq.5 splits the effective conductivity of the material into a gas and a solid contribution and includes a heat exchange term. Quintard et al. [35, 36] constructed pore-scale closure problems and solved them on a model porous medium composed of arrays of cylinders to study the variations of the effective properties as a function of the parameters of the problem. The results show that the effective thermal conductivities $\mathbf{k_{i,eff}}$ and the volumetric heat transfer coefficient h_v in the LTNE model vary as a function of the Peclet number Pe ($\rho_g c_{p,g} \mathbf{u} l_g / k_g$), the ratio of the solid thermal conductivity to the gas thermal conductivity and the gas-phase volume fraction ε_g. The determination of these tensors is not independent of h_v, therefore all these properties should be sought simultaneously.

The heat transfer coefficient may be determined either by pore-scale numerical simulation in representative geometries [44–46] or experimentally [40–42]. In the first method, the volume averaging theory is often applied to periodic structures, such are arrays of cylinders, to obtain h_v [44, 47]. With the progress of the resolution of computed microtomography and computer resources, pore-level numerical simulations are becoming a realistic approach to determine h_v [48–50]. Concerning the experimental method, the progress in optimisation algorithms and computer resources has allowed the general usage of inverse methods to infer the parameters with more accuracy [40, 42, 51, 52]. Using these two approaches, numerous correlations were obtained for the heat transfer coefficient h_v for a large variety of porous materials, like metal foams [40, 42, 53], ceramic foams [48, 52] and graphite foams [41] under diverse experimental conditions. A summary of the most widely used correlations and of their validity ranges is proposed in Table 1. However, none of the available correlations are suitable for carbon fiber felt due to its complex anisotropic microstructure.

In this context, the purpose of this article is to determine the effective conductivities and the heat transfer coefficients needed to inform the LTE and the LTNE models for Calcarb. In Section 2, the experimental facility and the test procedure are presented. In Section 3, the numerical inverse analysis method developed to infer the intrinsic parameters is described. It is based on a multi-objective optimization method to minimize errors between measured and predicted data. In Section 4, the experimental results and the estimated values of the LTE and LTNE parameters are presented and discussed. In section 5, a conclusion provides recommendations regarding the choice of a convective heat transfer model for Calcarb.

2. Experimental method

The experiments may be conducted using either a steady state [56, 57] or a transient regime [40, 42, 51, 58] approach. With the steady state approach, the sample is heated up and maintained at a given temperature. Cold gas is flown through the sample. The gas temperature is measured at the inlet and at the outlet of the sample. It is also measured within the sample when possible, that is, when the pores are large enough to allow measuring the gas temperature. The heat transfer coefficient is obtained by the analysis of the spatial evolution of the gas temperature. In the transient method instead, hot gas is used to heat a cold sample. The time evolution of the gas temperature is recorded upwind and downwind of the sample. This method is called the transient single blow technique (TSBT) [40, 41]. This method provides more information as one may measure the increase of temperature of the solid, which brings robustness for the inverse analysis. Last, but not least, as the solid and gas temperatures now both vary in space, one may infer simultaneously their effective thermal conductivities. The experimental facility presented in the following section is based on this method.

2.1. Experimental system and test procedure

A schematic drawing of the experimental setup that we have developed and an enlarged view of the test section, where thermocouple positions are shown, are displayed in Fig.3. The setup consists of a nitrogen gas inlet, a mass flow controller, a heat exchanger to heat the gas, and an insulated test section that contains the sample.

In the experiment, the first step is to set the flow rate of inlet gas. This value is controlled and measured by the mass flow controller (Bronkhorst F-201CV-020-AAD-11-Z) with a range of 1 to 4 liters/min, that is, a mass flow rate of Nitrogen ranging from 1.92×10^{-5} kg/s to 7.68×10^{-5} kg/s. The magnitude of the Darcy velocity u varies from 0.21 m/s to 0.84 m/s at room temperature ($T0 = 20°C$). The intrinsic gas velocity $\langle v_g\rangle^g$ inside the sample varies from 0.233 m/s to 0.932 m/s. When the gas temperature T_g rises to 80°C, v_g varies from 0.27 m/s to 1.08 m/s as the gas density ρ_g decreases from 1.15 kg/m^3 to 0.99 kg/m^3. This velocity range is consistent with the order of magnitude of 1 m/s of the pyrolysis gas velocity encountered in the TPS application, previously mentioned in the introduction.

The gas flows through a heat exchanger made of a Calcarb plug heated by a Ni-Cr wire wrapped around a quartz tube, as shown in Fig.3. The Ni-Cr wire is heated by Joule effect with a continuous power supply (Velleman LABPS3020). The red points in Fig.3 indicate the positions of the thermocouples (type K, 0.25 mm sheath diameter). The inlet and outlet gas temperatures, the tube surface temperature, and the temperature inside the sample are measured. The thermocouples are connected to a display data logger (Pico Technology TC-08) that records the temperature with a time step of 1.0 s. To measure the anisotropic properties of the materials, different experiments were performed by changing the orientation of the sampling (sample 1: Through-Thickness (TT) and sample 2: In-Plane (IP)). We performed X-ray scans for both samples to determine the exact location of the thermocouples (Fig. 4) in view of the inverse analysis. The sample dimension and the architectural properties of Calcarb are listed in Table 2. Due to the manufacturing process, there are clusters of fibers made of five to ten fibers. The mean diameter of the fiber clusters has been shown to be the most relevant characteristic length to compute the Reynolds number as it triggers the formations of eddies in the pores [31]. It will be used in the modeling section.

2.2. Experimental uncertainty analysis

There are two types of experimental uncertainties: the first one is the direct measurement error (caused by the experimental device), and the second one is the error arising from the measurement process.

Table 1
Empirical correlations for the heat transfer coefficient

Investigators	Media	Correlation	Remarks	Predicted h_v in (W/(m^3·K)) for Re =1
[54]	packed beds	$Nu_s = 2 + 1.1 Pr^{1/3} Re^{0.6}$	$Nu_s = h_s \cdot d_{par}/k_g$, $Re = \rho_g d_{par} u/\mu_g$ $1 \le Re \le 10^4$	1.83×10^7
[40]	metal foam	$Nu_v = 0.34 \varepsilon_g^{-2} Pr^{1/3} Re^{0.61}$	$Nu_v = h_v \cdot d_p^2/k_g$, $Re = \rho_g d_p u/\mu_g$ $20 \le Re \le 10^3$, $0.87 \le \varepsilon_g \le 0.97$	4.47×10^6 (extrapolated for $Re = 1$)
[42]	metal foam	$Nu_v = 0.3248 Re^{0.601}$	$Nu_v = h_v \cdot d_p^2/k_g$, $Re = \rho_g d_p u/\mu_g$ $1900 \le Re \le 7800$, $\varepsilon_g = 0.95$	3.89×10^6 (extrapolated for $Re = 1$)
[55]	ceramic foam	$Nu_v = 0.638 Re^{0.42}$	$Nu_v = h_v \cdot d_p^2/k_g$, $Re = \rho_g d_p u/\mu_g$ $24 \le Re \le 91$, $d_p = 0.29mm$	7.49×10^6 (extrapolated for $Re = 1$)
[56]	open cellular foam	$Nu_v = 0.124 (RePr)^{0.791}$	$Nu_v = h_v \cdot d_p^2/k_g$, $Re = \rho_g d_p u/\mu_g$ $1 \le Re \le 1000$	1.14×10^6
Current work	carbon fiber felt	not applicable (asymptotic behavior)	$Re = \rho_g d_{cl} u/\mu_g$ $1 \le Re \le 4$	$> 1 \times 10^8$ (local thermal equilibrium)

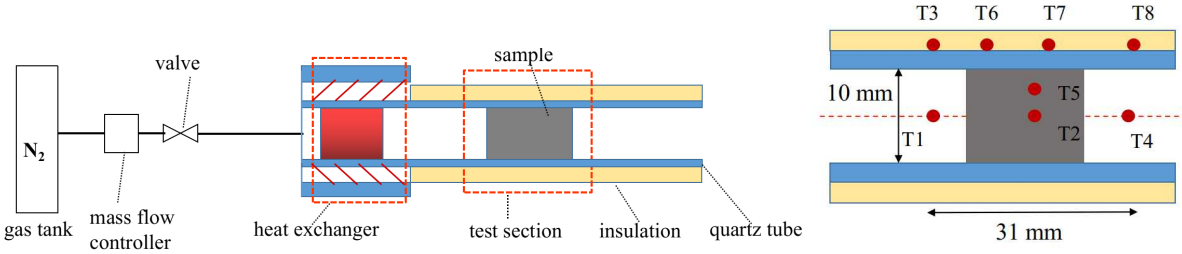

(a) experimental setup (b) test section part

Figure 3: Schematic diagram of the experimental system and enlarged view of the test section showing the thermocouple identification numbers

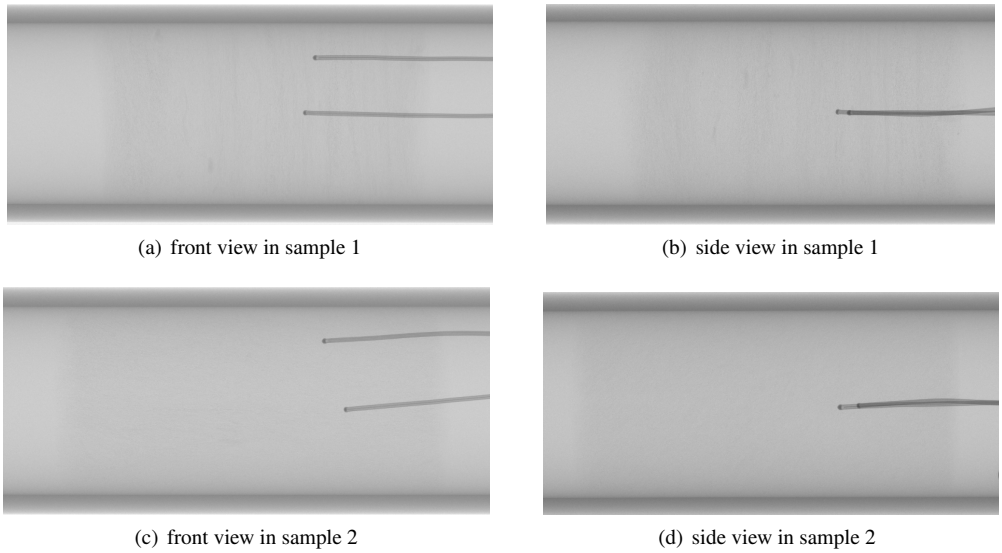

(a) front view in sample 1 (b) side view in sample 1

(c) front view in sample 2 (d) side view in sample 2

Figure 4: X-ray images of the thermocouple positions inside sample 1 (TT direction) and sample 2 (IP direction)

Table 2
Dimension and structural properties of the Calcarb samples

Sample dimensions (mm) diameter × length	Porosity ε_g	fiber diameter (μm) d_f	cluster diameter (μm) d_{cl}	fiber density (kg/m^3) ρ_s
10×17.4	0.9	10	80	1600

Table 3
The uncertainty analysis in the experimental measurements

	Range	Uncertainty
Temperature sensor (Pico Technology)	-270°C to +1820°C	± 0.2% of the reading
K-type thermocouple	-100°C to + 800°C	± 0.5 %
Volume mass flow controller	0 to 4 L/min	± 0.5 % of the reading
Temperature measurement in the flow region (due to the position of the thermocouple)	310 K to 360 K	0.1%

In this work, the ranges and uncertainties of the different sensors are reported in Table 3. Errors from the temperature measurement process are chiefly due to the positioning of the thermocouples in the flow region, upwind and downwind of the sample. In the sample, there is no uncertainty on the position as it is precisely measured with X-ray scans before testing. In the flow, the maximum temperature difference is 0.4 K within 2 mm of the front and rear of the measurement point. So the maximum resulting uncertainty on the temperature measurement in the flow regions is found to be 0.1%.

3. Parameter estimation method

Due to the complexity of the problem, we used numerical inverse analysis to estimate the quantities of interest. In the first subsection, we present the numerical model, and in the second subsection we detail the optimization algorithm used to infer the parameters.

3.1. Numerical model

For the purpose of parameter estimation, it is necessary to model the whole test section represented in Fig. 3. The numerical model is sketched in Fig. 5. It consists of a two-dimensional axisymmetric geometry where the different regions are identified as follows : flow1 (upwind flow field), sample (porous sample), flow2 (downwind flow field), tube (quartz tube), and thermocouple (downwind thermocouple). The choice of a two-dimensional axisymmetric geometry is discussed and justified in the Appendix.A.

3.1.1. Mathematical model and numerical implementation

The flow regions (flow1 and flow2) are modeled with the transient compressible laminar Navier-Stokes equations (conservation of mass, momentum, and energy). For the dense solid regions (tube, thermocouple), transient heat conduction is considered (energy conservation in a solid). In the porous sample region (sample), we consider either the LTE model (Eq.1) or the LTNE model (Eq.3). The Reynolds number based on the cluster diameter (d_{cl}) is defined as, $Re = \rho_g u d_{cl}/\mu_g$. Considering the gas velocity and density ranges provided in the previous section, Re is found to vary from 0.95 to 4.2. In a previous study, it was proved that Darcy's law remains valid with an error under 1% for $Re < 5$ [31]; hence, in this work, we will use Darcy's law. The coupling between the different regions is done by considering the conservation of mass and the continuity of temperatures and heat fluxes at the interfaces. The detailed expressions of the boundary conditions and of the initial conditions for the system of Eq.1 (LTE model) and the system of Eq.3 (LTNE model) are provided in Table 4 and Table 5 respectively. To simplify the notations, $\langle T_g \rangle^g$, $\langle T_s \rangle^s$, and $\langle T \rangle$, will be denoted by T_g, T_s and T respectively. In what follows, T is the temperature in the open flow regions (flow1 and flow2), T_g and T_s are the gas and solid temperatures in the sample and T_t is the temperature in the tube and thermocouple regions. The solid thermal conductivity in the tube and thermocouple regions are denoted by k_t. The imposed external boundary conditions are given by a second-order polynomial fitting of the experimental data.

The numerical model was implemented in finite volumes in the Porous material Analysis Toolbox based on OpenFOAM (PATO) [19] - where it is made available in open access. A multi-block approach is used, that is, in each region a different set of equations is solved at each time step with appropriate boundary conditions, computed from the mass and energy balances at the interfaces. The dense solid and flow region fields are computed using the conjugate heat transfer solver (chtMultiRegionFoam) of OpenFOAM 7 [59]. For the sample region, the pressure equation is solved semi-implicitly using first order schemes in time (Euler) and space (Gauss linear). The pressure gradient term is implicit and the other terms are explicit. The same approach is used for the energy equations, where the temperature terms are implicit and other quantities explicit. The equations are solved in series, with appropriate mesh refinement and time steps to

Table 4
Initial and boundary conditions of the LTE model

Region	Initial conditions		Boundary conditions		
flow1	$T = T0$	inlet $T = T1$ $p = \frac{u \cdot \mu_g \cdot L2}{\mathbf{K}} + p_{atm}$	flow1-tube interface $k_g \frac{\partial T}{\partial r} = k_t \frac{\partial T_t}{\partial r}$ $\frac{\partial p}{\partial r} = 0,\ u = 0$	flow1-sample interface $k_g \frac{\partial T}{\partial z} = k_{eff} \frac{\partial T}{\partial z}$ $p = p,\ u = \varepsilon_g \langle v_g \rangle^g$	
sample	$T = T0$	sample-flow1 interface $k_{eff} \frac{\partial T}{\partial z} = k_g \frac{\partial T}{\partial z}$ $p = p,\ \varepsilon_g \langle v_g \rangle^g = u$	sample-tube interface $k_{eff} \frac{\partial T}{\partial r} = k_t \frac{\partial T_t}{\partial r}$ $\frac{\partial p}{\partial r} = 0,\ \frac{\partial \langle v_g \rangle^g}{\partial r} = 0$	sample-flow2 interface $k_{eff} \frac{\partial T}{\partial z} = k_g \frac{\partial T}{\partial z}$ $p = p,\ \varepsilon_g \langle v_g \rangle^g = u$	
flow2	$T = T0$	flow2-sample interface $k_g \frac{\partial T}{\partial z} = k_{eff} \frac{\partial T}{\partial z}$ $\frac{\partial p}{\partial z} = 0,\ u = \varepsilon_g \langle v_g \rangle^g$	flow2-tube interface $k_g \frac{\partial T}{\partial r} = k_t \frac{\partial T_t}{\partial r}$ $\frac{\partial p}{\partial r} = 0,\ u$=0	flow2-therm interface $k_g \frac{\partial T}{\partial z} = k_t \frac{\partial T_t}{\partial z}$ $k_g \frac{\partial T}{\partial r} = k_t \frac{\partial T_t}{\partial r}$ $\frac{\partial p}{\partial r} = 0,\ \frac{\partial p}{\partial z} = 0$	outlet $p = p_{atm}$ u=0
therm-couple	$T_t = T0$	therm-flow2 interface $k_t \frac{\partial T_t}{\partial z} = k_g \frac{\partial T}{\partial z}$ $k_t \frac{\partial T_t}{\partial r} = k_g \frac{\partial T}{\partial r}$	outlet $\frac{\partial T_t}{\partial z} = 0$		
tube	$T_t = T0$	top T_t is a function of $T3$, $T6$, $T7$, $T8$	tube-flow1 interface $k_t \frac{\partial T_t}{\partial r} = k_g \frac{\partial T}{\partial r}$	tube-sample interface $k_t \frac{\partial T_t}{\partial r} = k_{eff} \frac{\partial T}{\partial r}$	tube-flow2 interface $k_t \frac{\partial T_t}{\partial r} = k_g \frac{\partial T}{\partial r}$

Table 5
Initial and boundary conditions of the LTNE model

Region	Initial conditions		Boundary conditions		
flow1	$T = T0$	inlet $T = T1$ $p = \frac{u \cdot \mu_g \cdot L2}{\mathbf{K}} + p_{atm}$	flow1-tube interface $k_g \frac{\partial T}{\partial r} = k_t \frac{\partial T_t}{\partial r}$ $\frac{\partial p}{\partial r} = 0,\ u = 0$	flow1-sample interface $k_g \frac{\partial T}{\partial z} = k_{g,eff} \frac{\partial T_g}{\partial z}$ $p = p,\ u = \varepsilon_g \langle v_g \rangle^g$	
sample	$T_g = T0$ $T_s = T0$	sample-flow1 interface $k_{g,eff} \frac{\partial T_g}{\partial z} = k_g \frac{\partial T}{\partial z},\ \frac{\partial T_s}{\partial z} = 0$ $p = p,\ \varepsilon_g \langle v_g \rangle^g = u$	sample-tube interface $\frac{\partial T_g}{\partial r} = 0,\ k_{s,eff} \frac{\partial T_s}{\partial r} = k_t \frac{\partial T_t}{\partial r}$ $\frac{\partial p}{\partial r} = 0,\ \frac{\partial \langle v_g \rangle^g}{\partial r} = 0$	sample-flow2 interface $k_{g,eff} \frac{\partial T_g}{\partial z} = k_g \frac{\partial T}{\partial z},\ \frac{\partial T_s}{\partial z} = 0$ $p = p,\ \varepsilon_g \langle v_g \rangle^g = u$	
flow2	$T = T0$	flow2-sample interface $k_g \frac{\partial T}{\partial z} = k_{g,eff} \frac{\partial T_g}{\partial z}$ $\frac{\partial p}{\partial z} = 0,\ u = \varepsilon_g \langle v_g \rangle^g$	flow2-tube interface $k_g \frac{\partial T}{\partial r} = k_t \frac{\partial T_t}{\partial r}$ $\frac{\partial T}{\partial z} = 0,\ u$=0 $\frac{\partial p}{\partial r} = 0$	flow2-therm interface $k_g \frac{\partial T}{\partial z} = k_t \frac{\partial T_t}{\partial z}$ $k_g \frac{\partial T}{\partial r} = k_t \frac{\partial T_t}{\partial r}$ $\frac{\partial p}{\partial r} = 0,\ \frac{\partial p}{\partial z} = 0$	outlet $p = p_{atm}$ u=0
therm-couple	$T_t = T0$	therm-flow2 interface $k_t \frac{\partial T_t}{\partial z} = k_g \frac{\partial T}{\partial z}$ $k_t \frac{\partial T_t}{\partial r} = k_g \frac{\partial T}{\partial r}$	outlet $\frac{\partial T_t}{\partial z} = 0$		
tube	$T_t = T0$	top T_t is a function of $T3$, $T6$, $T7$, $T8$	tube-flow1 interface $k_t \frac{\partial T_t}{\partial r} = k_g \frac{\partial T}{\partial r}$	tube-sample interface $k_t \frac{\partial T_t}{\partial r} = k_{s,eff} \frac{\partial T_s}{\partial r}$	tube-flow2 interface $k_t \frac{\partial T_t}{\partial r} = k_g \frac{\partial T}{\partial r}$

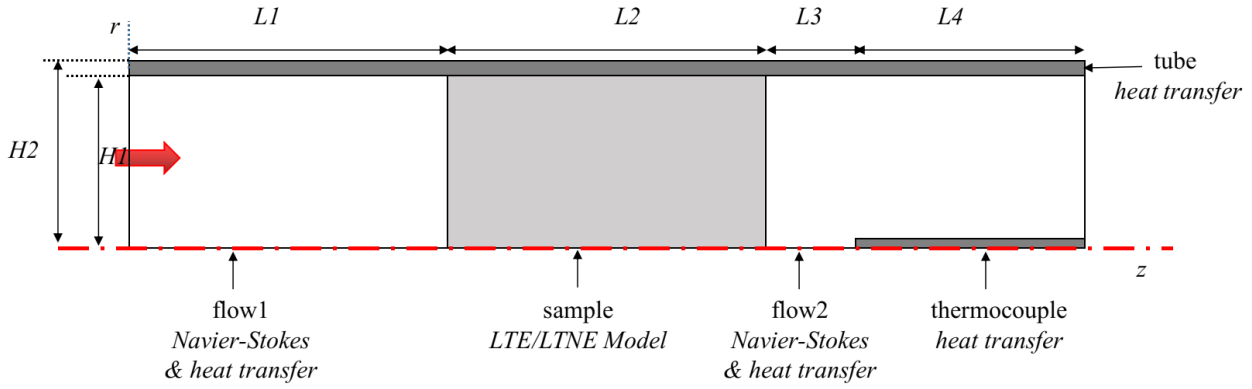

Figure 5: Two-dimensional axisymmetric numerical model of the test section

guaranty that the order of convergence is reached, as described in Appendix.B.

3.1.2. Thermal properties of Calcarb and of Nitrogen

The effective conductivity of Calcarb in static conditions was measured in IP and TT directions using the Transient Plane Sources technique (Hot Disk, TPS 3500) [60]. At room temperature, these values are ($k_{eff,IP,static}$=0.399) and ($k_{eff,TT,static}$=0.212) W/(m·K) with an uncertainty of 5 % . The effective conductivity tensor $\mathbf{k_{eff,static}}$ at room temperature may be defined in cylindrical coordinates as shown in Eq.6, where z represents the TT direction. For the same type of fiber materials (FiberForm), the mean thermal conductivity values obtained in the literature [61] are 0.392 and 0.167 W/(m·K) in the IP and TT directions. In these materials, as well as in our measurement, the thermal conductivity value in the IP direction is nearly twice the value obtained in the TT direction.

$$\mathbf{k_{eff,static}}_{\text{, room temperature}} = \begin{bmatrix} k_{eff,IP,static} & 0 & 0 \\ 0 & k_{eff,IP,static} & 0 \\ 0 & 0 & k_{eff,TT,static} \end{bmatrix}_{(r,\theta,z)} = \begin{bmatrix} 0.399\pm5\% & 0 & 0 \\ 0 & 0.399\pm5\% & 0 \\ 0 & 0 & 0.212\pm5\% \end{bmatrix}_{(r,\theta,z)} \tag{6}$$

Fig. 6 shows the variations as a function of temperature of the nitrogen gas thermal conductivity k_g and heat capacity $c_{p,g}$, and of the effective thermal conductivity $k_{eff,IP,static}$, $k_{eff,TT,static}$ and heat capacity $c_{p,s}$ of the Calcarb sample. Presented data for the gas thermal conductivity k_g and heat capacity $c_{p,g}$ were obtained from the literature [62]. The effective thermal conductivities $k_{eff,IP,static}$ and $k_{eff,TT,static}$ were measured at 291 K (room temperature), 301 K, 311 K, and extended linearly to 370 K. The solid heat capacity $c_{p,s}$ of the Calcarb sample were obtained from a recently published work [63].

When considering the dispersion effect due to the flow of gas [64, 35], the effective conductivity $\mathbf{k_{eff}}$ used in the LTE model (Eq.1) and presented in Eq.2 may be defined in cylindrical coordinates as shown in Eq.7, where $k_{dis,1}$ and $k_{dis,2}$ represent the two components of dispersion term $\mathbf{k_{dis}}$ in the horizontal and transverse flow directions. For the purpose of carrying out the inverse analysis, we use coefficients $c1$ and $c2$ multiplied by the effective conductivity of Calcarb under static conditions to represent the components of effective conductivity. The solid effective thermal conductivity $\mathbf{k_{s,eff}}$, and gas effective thermal conductivity $\mathbf{k_{g,eff}}$ used in the LTNE model (Eq.3) and presented in Eq.5 may be sought as shown in Eq.8 and Eq.9, where $c3 \cdot k_g$ and $c4 \cdot k_g$ represent the two components of tortuosity term $\mathbf{k_{tor}}$, $c5$ and $c6$ indicate the two components of dispersion term $\mathbf{k_{dis}}$. The parameters $c1$ to $c6$ will be optimized as described in section 3.2.

$$\mathbf{k_{eff}} = \begin{bmatrix} k_{eff,IP,static}+k_{dis,1} & 0 & 0 \\ 0 & k_{eff,IP,static}+k_{dis,1} & 0 \\ 0 & 0 & k_{eff,TT,static}+k_{dis,2} \end{bmatrix}_{(r,\theta,z)} = \begin{bmatrix} c1\cdot k_{eff,IP,static} & 0 & 0 \\ 0 & c1\cdot k_{eff,IP,static} & 0 \\ 0 & 0 & c2\cdot k_{eff,TT,static} \end{bmatrix}_{(r,\theta,z)} \tag{7}$$

$$\mathbf{k_{s,eff}} = \begin{bmatrix} k_{eff,IP,static}-\varepsilon_g k_g-c3\cdot k_g & 0 & 0 \\ 0 & k_{eff,IP,static}-\varepsilon_g k_g-c3\cdot k_g & 0 \\ 0 & 0 & k_{eff,TT,static}-\varepsilon_g k_g-c4\cdot k_g \end{bmatrix}_{(r,\theta,z)} \tag{8}$$

$$\mathbf{k_{g,eff}} = \begin{bmatrix} \varepsilon_g k_g+c3\cdot k_g+c5 & 0 & 0 \\ 0 & \varepsilon_g k_g+c3\cdot k_g+c5 & 0 \\ 0 & 0 & \varepsilon_g k_g+c4\cdot k_g+c6 \end{bmatrix}_{(r,\theta,z)} \tag{9}$$

3.2. Optimization process

An inverse analysis method was used to infer the intrinsic parameters from experimental measurements to minimize errors between measured and predicted data. We possess four data sequences $\{T1^i\}_{i=0}^n$, $\{T4^i\}_{i=0}^n$, $\{T2^i\}_{i=0}^n$, $\{T5^i\}_{i=0}^n$ that correspond to the measured temperatures collected at every time step indicated by the index i, respectively at the inlet, at the outlet and inside the sample (see Fig.3). The transient inlet gas temperature data $T1$ is fitted into a second-order polynomial using least squares, and it is used as a boundary condition. The objective function S for the optimization processes is defined as the average of the root mean squared relative error between

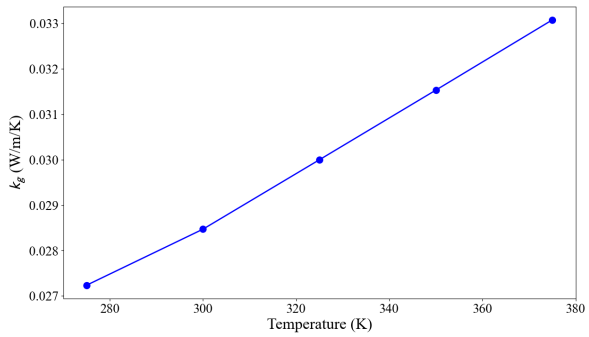

(a) gas thermal conductivity

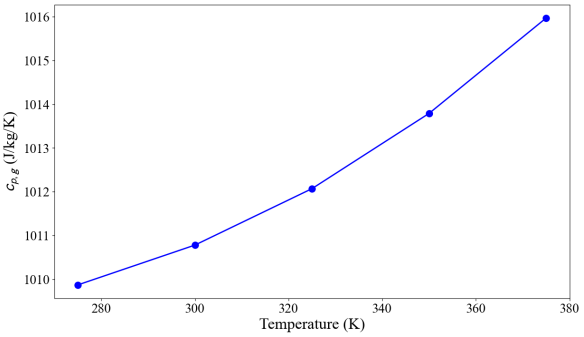

(b) gas heat capacity

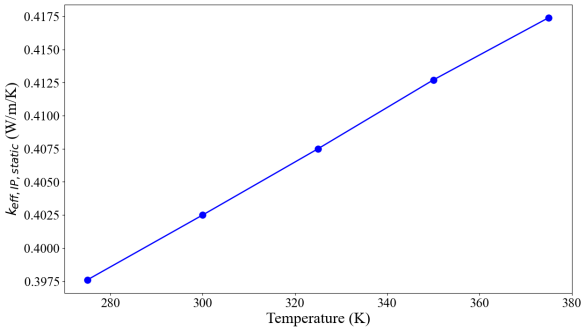

(c) effective thermal conductivity in IP direction

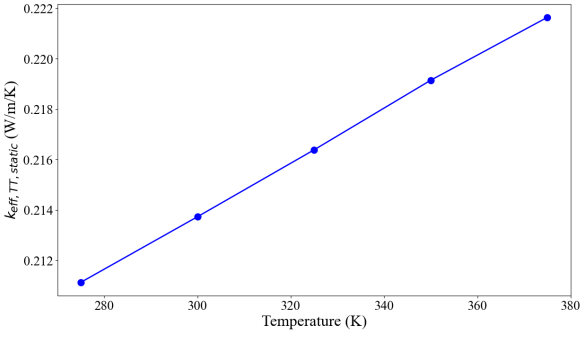

(d) effective thermal conductivity in TT direction

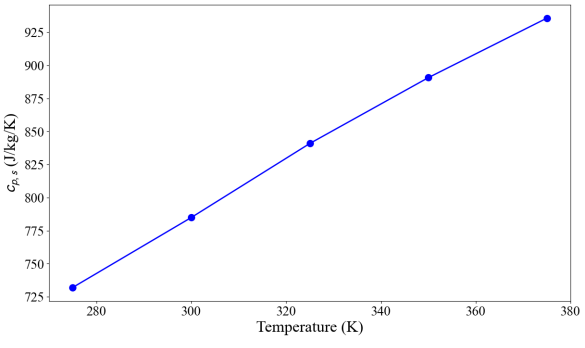

(e) solid heat capacity

Figure 6: Thermal conductivity and heat capacity as a function of temperature for Nitrogen and for the solid phase of Calcarb

measured and predicted temperatures on the three positions already mentioned ($T4$, $T2$, $T5$):

$$S = \frac{1}{3}\left(\sqrt{\frac{1}{n}\sum_{i=1}^{n}\left(\frac{T4^i_{num} - T4^i}{T4^i}\right)^2} + \sqrt{\frac{1}{n}\sum_{i=1}^{n}\left(\frac{T2^i_{num} - T2^i}{T2^i}\right)^2}\right. \tag{10}$$

$$\left. + \sqrt{\frac{1}{n}\sum_{i=1}^{n}\left(\frac{T5^i_{num} - T5^i}{T5^i}\right)^2}\right) \tag{11}$$

The minimization of S was performed with the Design Analysis Kit for Optimization and Terascale Applications (DAKOTA) [65]. A combination of the global optimization method DIviding RECTangles algorithm (NCSU DIRECT) [66] and of the local optimization method Adaptive nonlinear least-squares algorithm (NL2SOL) [67] were used. NCSU DIRECT, as a global optimization algorithm, always find the global optimum of a function within a given domain given enough function evaluations and highly sensitive stopping criteria. However, this exhaustive search can be computationally expensive to reach the minimum [66]. Therefore, if final convergence becomes slow, NL2SOL is used to speed-up convergence within the sub-region

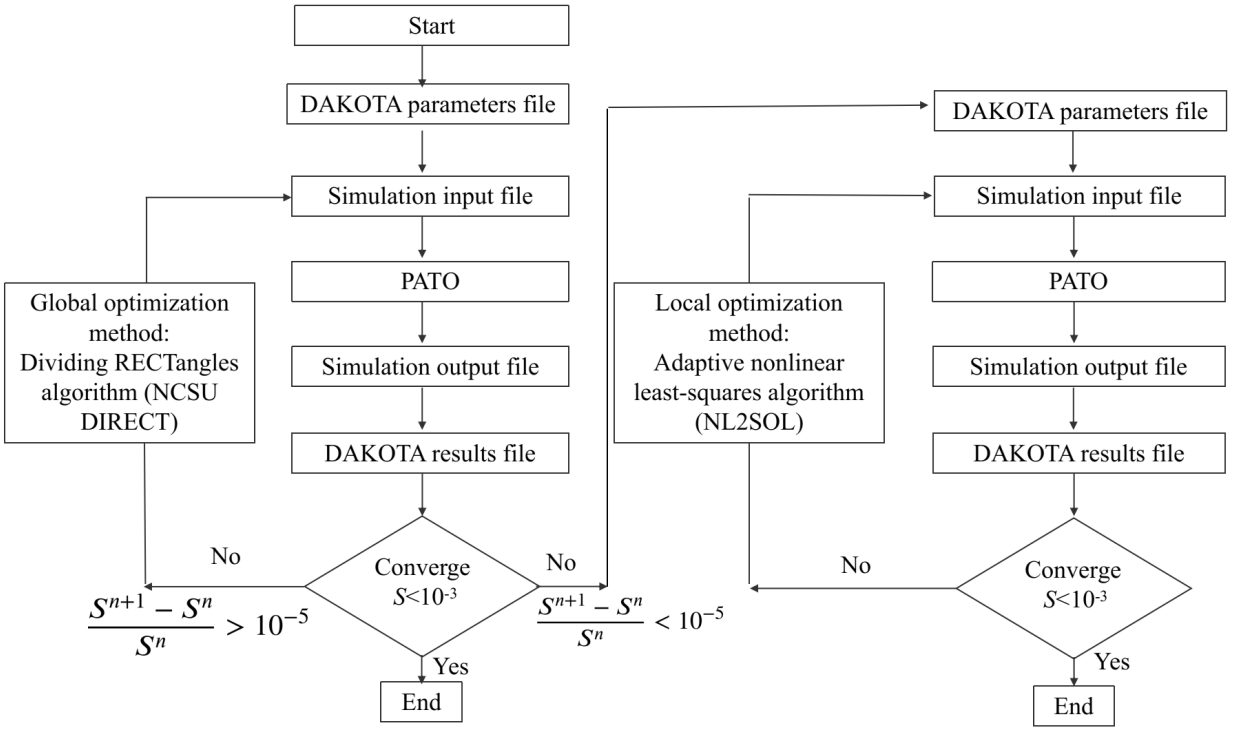

Figure 7: The steps of optimization process

identified by NCSU DIRECT. An overview of this optimization strategy is presented in Fig.7. It will be further explained taking examples of applications to LTE and LTNE model optimisations in the next section.

4. Results and discussions

Results of measured and predicted temperatures are reported in this section. In the first subsection, the volumetric heat transfer coefficient h_v used in the LTNE model is determined and the pressure, velocity, and temperature fields predicted with the LTNE model are presented. The second subsection focuses on assessing the validity of the LTE model in the conditions of the experiment.

4.1. Determination of the volumetric heat transfer coefficient h_v used in the LTNE model

Fig.8 presents a typical comparison of the measured and predicted results, where measured results are represented by dots, and predicted results obtained by solving the LTNE model are represented by solid and dashed lines. The recorded inlet gas temperature, sample temperature at two locations (T2, T5), and outlet gas temperature are a function of time. The temperature data presented is the subset used in the optimization process. For the predicted results, solid temperatures are represented with solid lines and gas temperatures with dashed lines. The procedure for solving h_v is then presented.

According to the model presented in the previous section, there are five parameters to optimize : h_v, $c3$, $c4$, $c5$ and $c6$. Studies have indicated that the tortuosity terms represented by $c3 \cdot k_g$ and $c4 \cdot k_g$ in $\mathbf{k}_{\mathbf{g,eff}}$ are significantly smaller than the dispersion terms represented by $c5$ and $c6$ [43, 35]. One can also notice that when summing the effective conductivity of the solid (Eq.8) and the effective conductivity of the gas (Eq.9), the tortuosity terms cancel each other. Due to the combination of these two properties, the sensitivity on $c3$ and $c4$ becomes very small when approaching local thermal equilibrium (that - we will see - is reached in our case). Therefore, in what follows, we set the values of $c3$ and $c4$ to zero and run the optimization on three parameters: h_v, $c5$, and $c6$.

As a large number of simulations were carried out, a representative case (1m/s in the TT-direction) was selected to demonstrate the optimisation procedure and to present the two-dimensional simulation results. In order to choose minimum and maximum values of the parameters to be optimized, orders of magnitude are sought from the literature. We used the correlations provided by Essence et al. [64] for packed beds and obtained estimates of the dispersion terms of about 0.1 $\mathrm{W/(m \cdot K)}$ and of the volumetric heat transfer coefficient h_v of the order of 10^7 $\mathrm{W/(m^3 \cdot K)}$ for a Reynolds number of 4. Taking advantage of the global optimization ability of the NCSU DIRECT algorithm, we respectively set $c5$, $c6$, and h_v from 0 to 0.5 $\mathrm{W/(m \cdot K)}$, 0 to 0.5 $\mathrm{W/(m \cdot K)}$, and 10^6 to 10^{11} $\mathrm{W/(m^3 \cdot K)}$. Convergence ($S < 0.001$) was reached after 115 iterations of the global optimization algorithm (in this case local optimisation was not necessary).

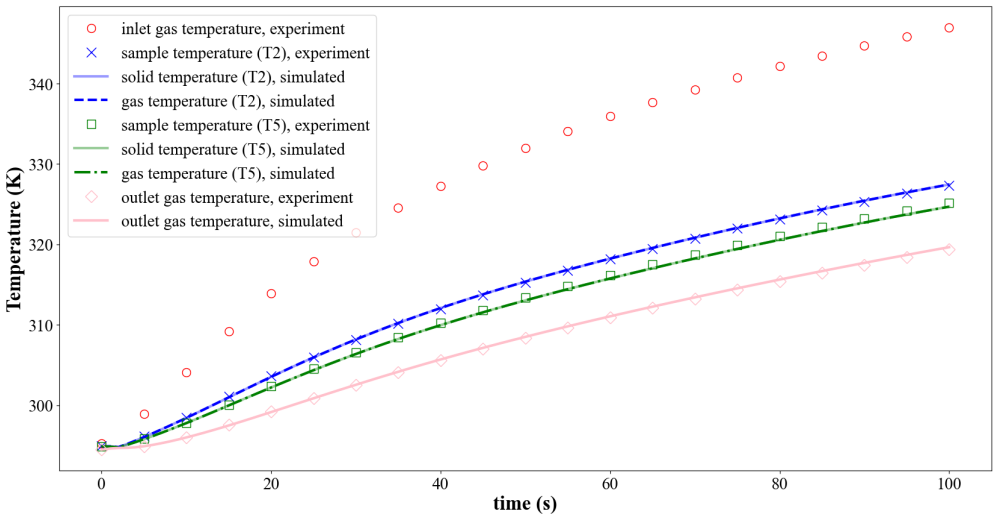

Figure 8: The comparison of predicted and measured temperature in TT direction ($qm = 7.68 \times 10^{-5}$ kg/s).

Fig.9 shows the influence of the three variables (h_v, $c5$ and $c6$) on the error S. The grey scale indicates the value of $c6$, and the size of points indicates the value of S. As shown in Fig.9, when S is below 0.0025, the values of $c6$ are distributed between 0.05 to 0.17 W/(m · K), the values of $c5$ are concentrated around on 0.115 W/(m · K), and the values of h_v span four orders of magnitude ranging from 10^7 to 10^{11} W/(m^3·K). To analyse further the behavior of the error when varying h_v, we set $c5$ to 0.115 W/(m · K) and $c6$ to the average of the range obtained above, that is, 0.11 W/(m · K). As shown in Fig.10, S displays an asymptotic behavior. Beyond a critical value of h_v of 10^8 W/(m^3·K), a change in h_v does not affect the error. This is due to the fact that local thermal equilibrium is reached. The temperature predictions for $h_v = 10^8$ W/(m^3·K) are plotted in Fig.8; the predicted solid and gas temperatures overlap at the thermocouple positions. To present further the overall behavior of the sample, the color maps of the simulation results are now presented.

Figs. 11, 12 and 13 show the pressure, velocity, and temperature fields in the test section at 100 s. Fig.14 shows the temperature fields inside the sample region at 100 s. The pressure gradient in the flow1 and flow2 regions is very small, whereas in the sample region the pressure gradient is driven by the permeability of the sample.

In the flow1 and flow2 regions the gas flow is laminar ($Re = \rho_g u D/\mu_g = 1.17{\times}0.84{\times}0.01/0.000019 = 517$) and the velocity distribution is in agreement with Poiseuille's law where it is fully developed (entrance of flow1, exit of flow2). The gas velocity inside the sample $\langle \mathbf{v_g} \rangle^{\mathbf{g}}$ is equal to the Darcy velocity $\mathbf{u}$ divided by the porosity ε_g. The gas velocity profile can be considered unidirectional in the sample.

In the sample region, the difference between the local average gas and solid temperatures T_g and T_s is negligible. This indicates that in this case, for which the value of h_v is large ($h_v = 10^8$W/m^3 K), heat transfer between the gas and the solid phases is important and local thermal equilibrium is reached.

The same methodology was applied for the other studied cases (flow rates from qm=1.9×10^{-5} kg/s to qm=7.68×10^{-5} kg/s for both TT and IP directions) and the same conclusions were reached, that is, h_v is greater than or equal to 10^8, in the conditions of the experiment (no chemical reactions, unity Reynolds number) and the local thermal equilibrium assumption holds.

4.2. Validation of the LTE model

The objective of this section is to infer the effective thermal conductivity $\mathbf{k_{eff}}$ and to validate the LTE model. Experimental data are presented using dots in Fig.15 and Fig.16. As shown in Eq.7, there are two dimensionless coefficients $c1$ and $c2$ to optimize to infer the effective thermal conductivity $\mathbf{k_{eff}}$. They are respectively linked to $k_{eff,IP}$ and $k_{eff,TT}$. As mentioned in Subsection 3.2, the global optimization algorithm (NCSU DIRECT) and the local optimization algorithm (NL2SOL) are used. To guide the choice of the minimum and maximum for the parameters to optimize, we used the correlations provided by Quintard et al. [36] for packed beds and obtained estimates of the maximum dispersion terms of about 0.1 W/(m K) for a Reynolds number of 4, that is, $0.25{\cdot}k_{eff,IP,static}$ or $0.47 \cdot k_{eff,TT,static}$. The effective conductivity equals the effective conductivity in static conditions plus the dispersion terms. As a first step, we perform global optimization with the NCSU DIRECT algorithm with ranges for $c1$ and $c2$ between 0.1 and 3. During the optimization process, if the NCSU DIRECT algorithm reaches the convergence criterion ($S < 10^{-3}$), the optimisation ends. If the global optimisation fails to converge ($(S^{n+1} - S^n)/S^n < 10^{-5}$), the NL2SOL algorithm should be manually defined within a subregion which is obtained from the NCSU DIRECT, such that we can eventually achieve the final convergence.

Fig.17 shows the optimization results of $(c1, c2)$ in the IP and TT directions for the different mass-flow rates of the study. The errors S obtained from the NCSU DIRECT and NL2SOL algorithms are respectively represented with squares and dots.

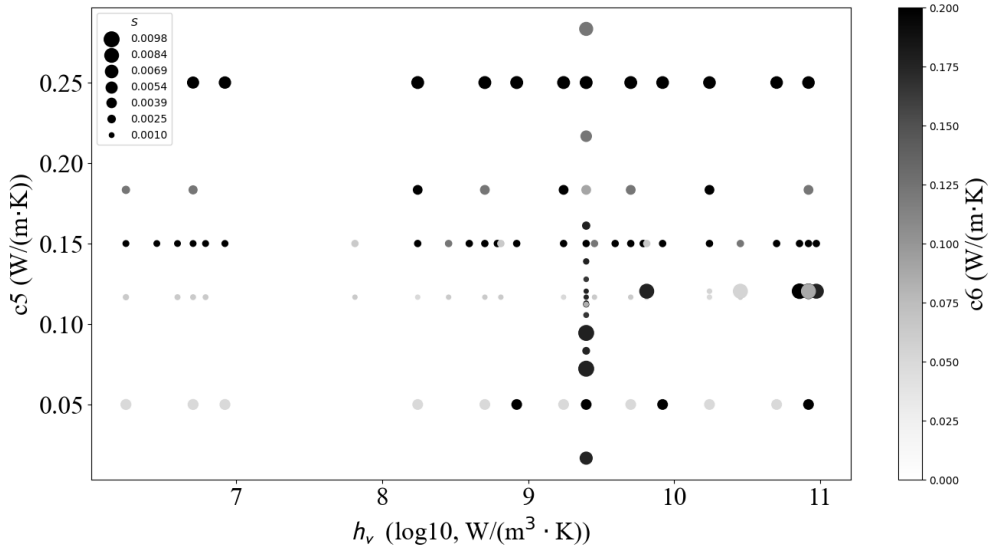

Figure 9: The influence of three variables on the error S, qm=7.68×10^{-5} kg/s

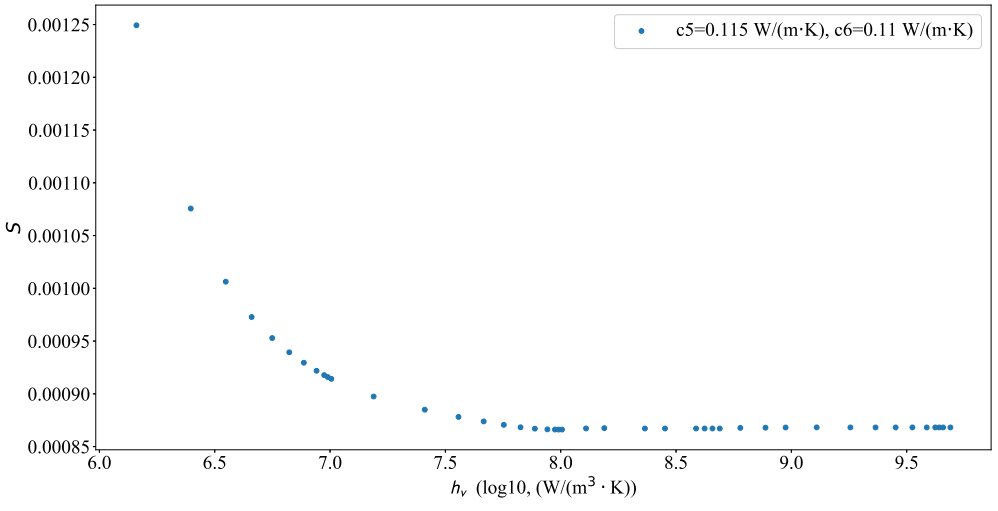

Figure 10: The influence of h_v on the error S

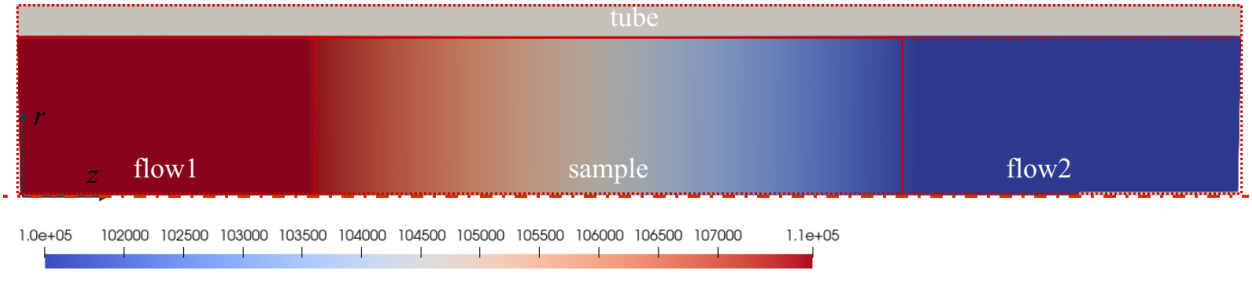

Figure 11: Pressure p (Pa) distribution predicted with the LTNE model

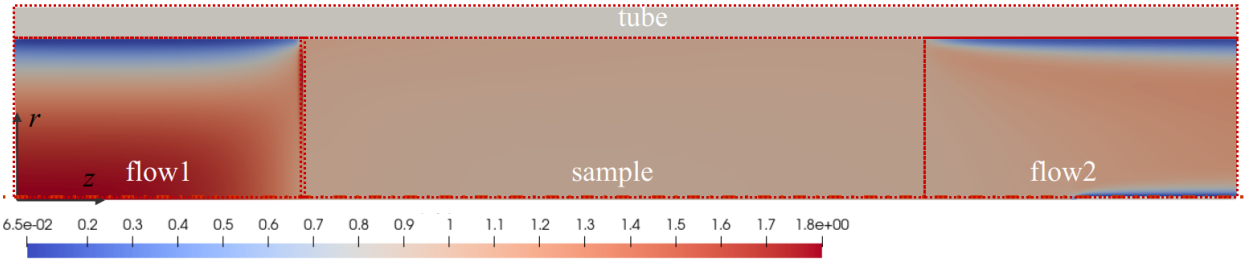

Figure 12: Velocity magnitude u (m/s) predicted with the LTNE model

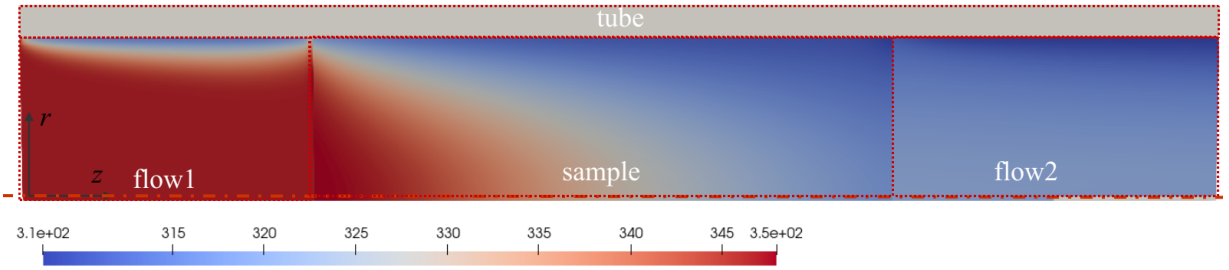

Figure 13: Gas temperature T (K) predicted with the LTNE model

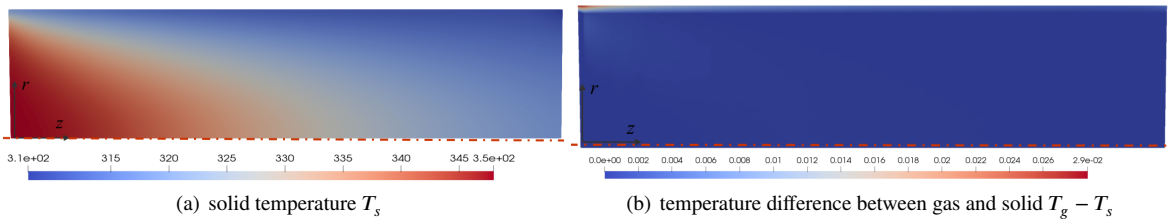

(a) solid temperature T_s (b) temperature difference between gas and solid $T_g - T_s$

Figure 14: Solid temperature and the difference $T_g - T_s$ (in K) in the sample region predicted with the LTNE model

Their sizes indicate the value of error S. Figs.17(a) and (b) respectively correspond to the mass-flow rate of qm=1.9×10^{-5} kg/s in the IP and TT directions; NCSU DIRECT converges after approximately 90 iterations. For the other six cases in Figs.17(c)-(h), the final convergence was reached after around 60 iterations of NCSU DIRECT and then around 30 iterations of NL2SOL.

For the optimization in the IP direction as shown in Fig.17 (left), $c1$ and $c2$ are respectively associated with the component of the effective thermal conductivity in the horizontal and transverse flow directions. When the error $S < 0.001$, the values of $c2$ are distributed between 1.45 and 2.03. More specifically, for the four mass-flow rates, they are respectively 1.50 ± 0.05, 1.59 ± 0.05, 1.85 ± 0.05, and 1.98 ± 0.05. However, the sensitivity is smaller for $c1$ because there is less temperature gradient in the flow direction. For the optimization in the TT direction as shown in Fig.17 (right), oppositely, $c1$ and $c2$ are respectively associated with the transverse and horizontal flow directions. When the error $S < 0.001$, the values of $c1$ span from 1.05 to 1.34. Precisely, they are respectively 1.08 ± 0.03, 1.12 ± 0.03, 1.19 ± 0.03, and 1.31 ± 0.03. Similarly with the previous case, the sensitivity of $c2$ is small. To sum-up, when the error S converges to the level of 10^{-4}, the ranges of the effective thermal conductivity from the optimization solution are given in Table 6. The effective thermal conductivity is found to increase with the Peclet number Pe as expected from the theory presented in the introduction.

Fig.15 and Fig.16 show the comparisons between the measured and predicted temperatures in the IP and TT directions with different mass-flow rates. The solid line represents the predicted temperature curve, obtained by minimizing the error S. Taking Fig.15 (d) as an example, the values of the error S equals 8.01×10^{-4}, which is the average of 8.20×10^{-4}, 7.53×10^{-4}, and 8.30×10^{-4} corresponding to the three positions: T2, T5, and the outlet point. For reference, the temperature difference between the predicted and measured values is around 0.25 K at the outlet point. This implies that the LTE model may be used with a good level of accuracy to model materials such as Calcarb in the conditions of our experiments, that is, for non reactive flows and Reynolds numbers up to 4.

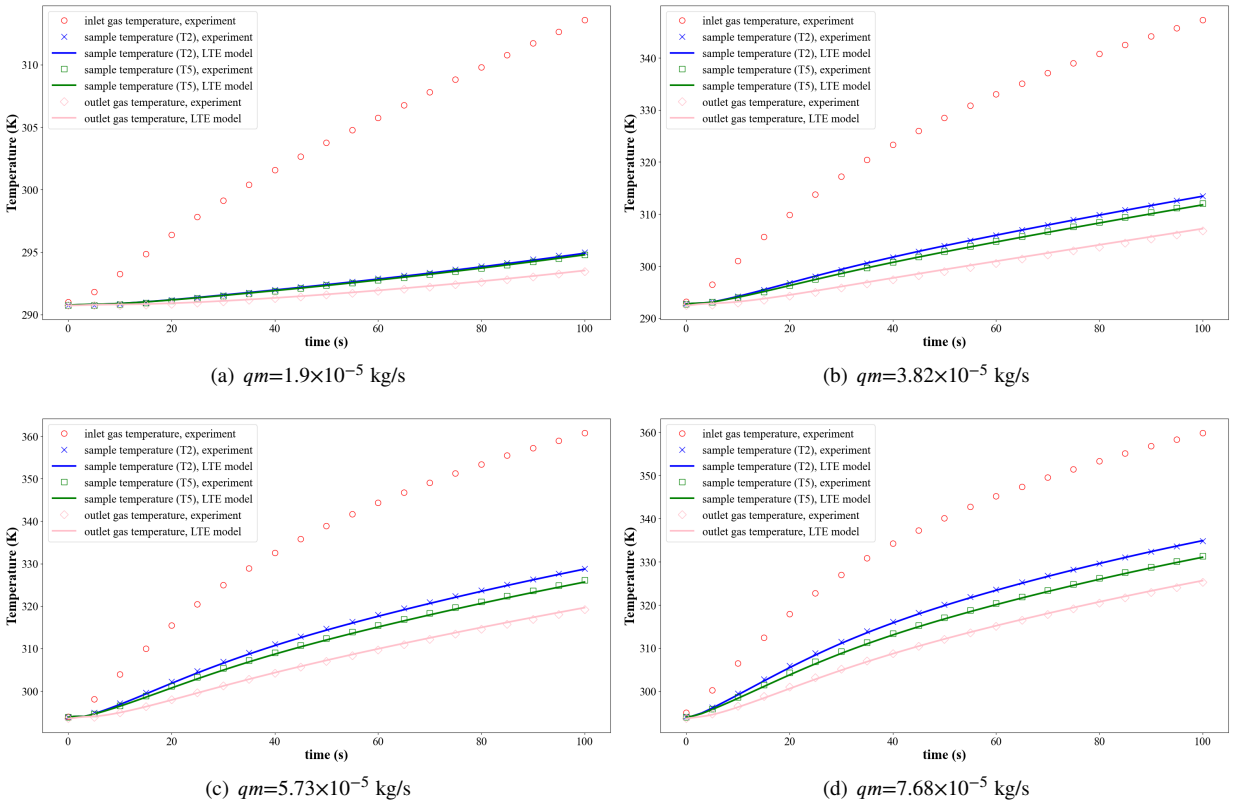

(a) qm=1.9×10^{-5} kg/s

(b) qm=3.82×10^{-5} kg/s

(c) qm=5.73×10^{-5} kg/s

(d) qm=7.68×10^{-5} kg/s

Figure 15: Comparison of predicted and measured temperatures in IP direction with the LTE model.

Table 6
The value of $\mathbf{k_{eff}}$, and error S between LTE model and measured values for different mass-flow rates

Flow direction	qm (kg/s)	Pe	$k_{eff,IP}$ (W/(m · K))	LTE $k_{eff,TT}$(W/(m · K))	S
IP	1.9×10^{-5}	0.7	0.399±0.11	0.319±0.01	1.57×10^{-4}
	3.82×10^{-5}	1.4	0.399±0.12	0.339±0.01	5.17×10^{-4}
	5.73×10^{-5}	2.1	0.399±0.13	0.396±0.01	8.51×10^{-4}
	7.68×10^{-5}	2.8	0.399±0.19	0.422±0.01	8.01×10^{-4}
TT	1.9×10^{-5}	0.7	0.432±0.01	0.318±0.11	4.50×10^{-4}
	3.82×10^{-5}	1.4	0.448±0.01	0.318±0.11	7.85×10^{-4}
	5.73×10^{-5}	2.1	0.475±0.01	0.360±0.11	8.80×10^{-4}
	7.68×10^{-5}	2.8	0.523±0.01	0.360±0.11	6.93×10^{-4}

5. Conclusions

The objective of this work was to study coupled heat and mass transfer in Calcarb, a carbon fiber preform used as insulator in many applications, and, in particular, in TPS materials. The TPS community has recently been questioning the validity of the local thermal equilibrium hypothesis and was lacking experimental data to conclude. In this work we designed a new experimental facility, based on the transient single blow technique, to determine the heat transfer coefficient h_v of low density porous materials. Experiments were conducted with nitrogen for Reynolds numbers representative of the TPS application (1 to 4) for both in-plane (IP) and through-thickness (TT) orientations. Parameter estimations were carried out using numerical inverse analysis. Local thermal equilibrium (LTE) and local

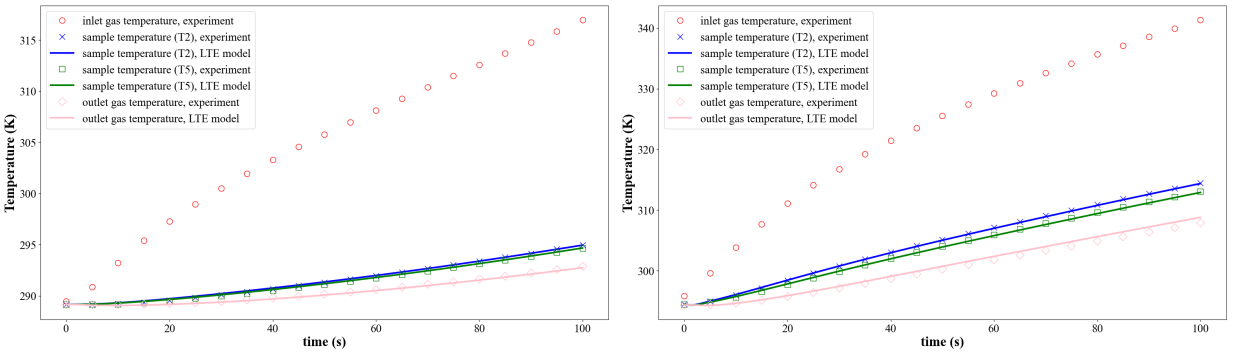

(a) qm=1.9×10^{-5} kg/s

(b) qm=3.82×10^{-5} kg/s

(c) qm=5.73×10^{-5} kg/s

(d) qm=7.68×10^{-5} kg/s

Figure 16: Comparison of predicted and measured temperatures in TT direction with the LTE model.

thermal non-equilibrium (LTNE) models have been employed to investigate heat and mass transfer phenomena. The numerical model was implemented in finite volumes in the Porous material Analysis Toolbox based on Open-FOAM (PATO). Two optimization algorithms were employed in this work: a global optimization method, NCSU DIRECT, and a local optimization method, NL2SOL to minimize the error between measured and predicted temperatures. The optimization process was performed with the Open Source optimization software Dakota. The results revealed that the value of the heat transfer coefficient h_v was greater than or equal to 10^8 W/(m^3·K), demonstrating that for non-reactive flows and for Reynolds numbers up to 4 the local thermal equilibrium assumption holds. The maximum error S between measured and predicted (LTE) results is 8.8×10^{-4}. This implies that the LTE model may be used with a good level of accuracy to model materials such as Calcarb in the conditions of our experiments. One should note that although the LTNE model is not necessary in this case, the value of h_v determined in this work is useful for porous media applications such as ablative heat-shield design, where chemical non-equilibrium may challenge local thermal equilibrium [68]. Pioneering works, such as the study of Scoggins et al. [29], may now be revisited in the light of this newly available data.

Declaration of Competing Interest

The authors declare that they have no known competing financial interests or personal relationships that could have appeared to influence the work reported in this paper.

Acknowledgements

This work was supported by the China Scholarship Council (CSC) program (No. 201907040064).

A. Appendix. Validation of the two-dimensional axisymmetric model in the IP direction

In this work, the numerical model consists of a two-dimensional axisymmetric geometry. For the flow in the TT direction, the radial direction is IP and the sample has isotropic properties in the whole radial plane. It is adapted to use a two-dimensional axisymmetric geometry to represent the three-dimensional geometry. However, for the flow in the IP direction, the radial direction contains both TT and IP, and the sample has anisotropic properties in the whole radial plane. A three-dimensional simulation is performed to validate the simulation results of the two-dimensional axisymmetric geometry on the

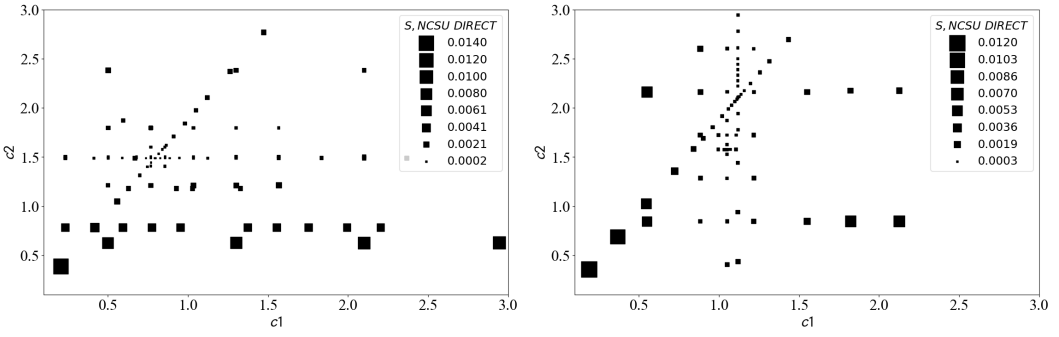

(a) qm=1.9×10^{-5} kg/s

(b) qm=1.9×10^{-5} kg/s

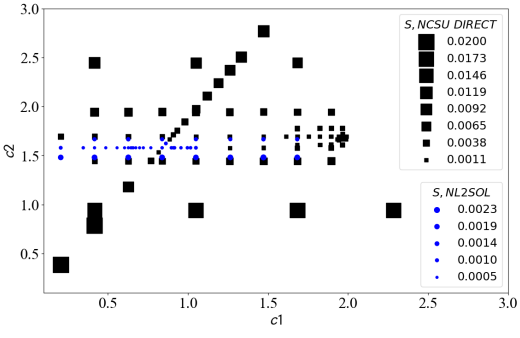

(c) qm=3.82×10^{-5} kg/s

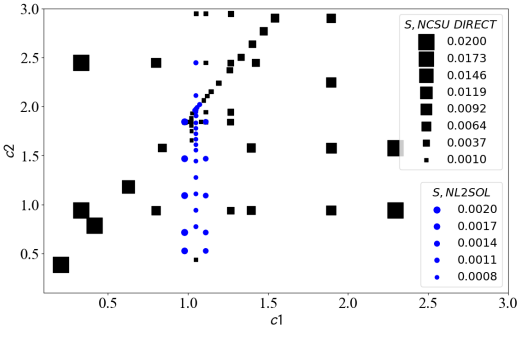

(d) qm=3.82×10^{-5} kg/s

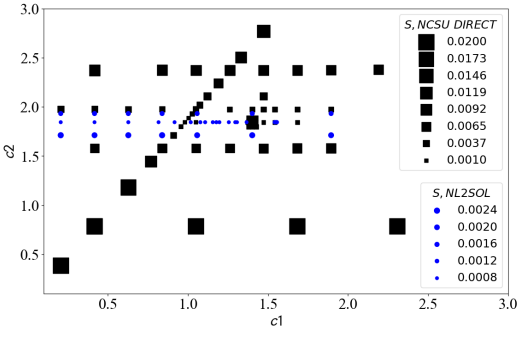

(e) qm=5.73×10^{-5} kg/s

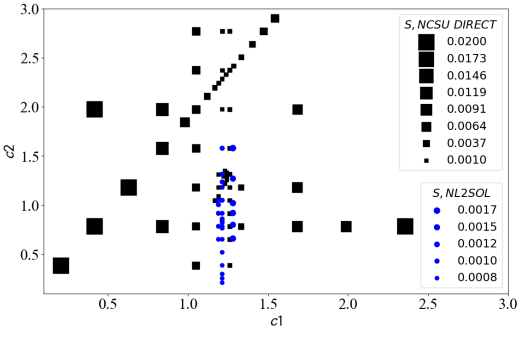

(f) qm=5.73×10^{-5} kg/s

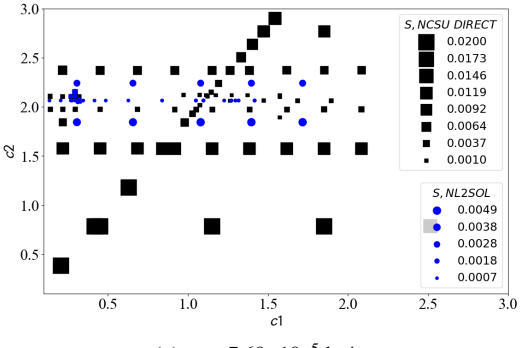

(g) qm=7.68×10^{-5} kg/s

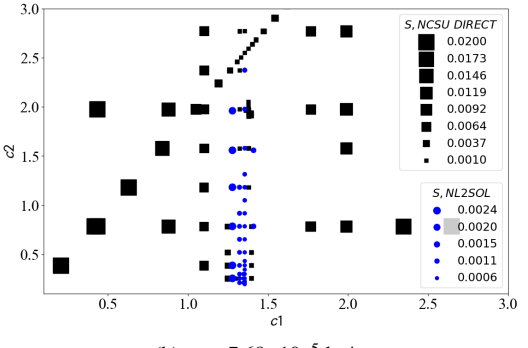

(h) qm=7.68×10^{-5} kg/s

Figure 17: The optimization results in IP direction (left) and TT direction (right) in the LTE model

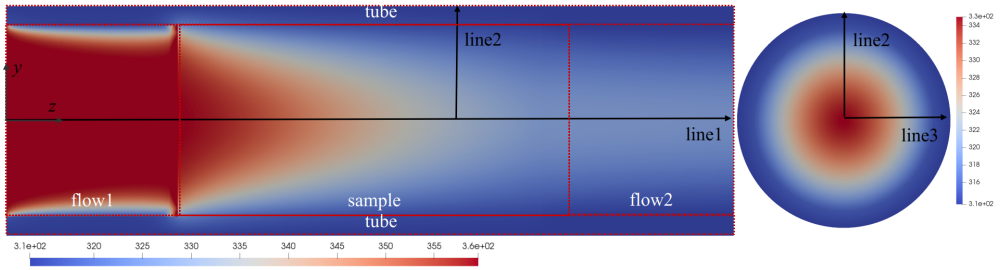

(a) Temperature fields (K) in the yz plane (x=0 m) and xy plane (z=0.021 m) in three-dimensional model

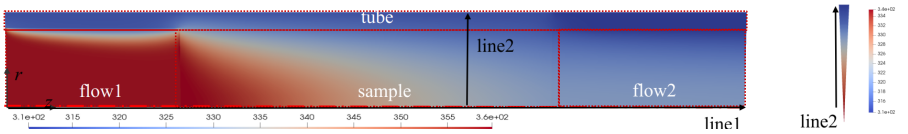

(b) Temperature fields (K) in the rz plane and r plane (z=0.021 m) in two-dimensional axisymmetric model

Figure 18: Temperature fields (K) in three-dimensional and two-dimensional axisymmetric numerical model

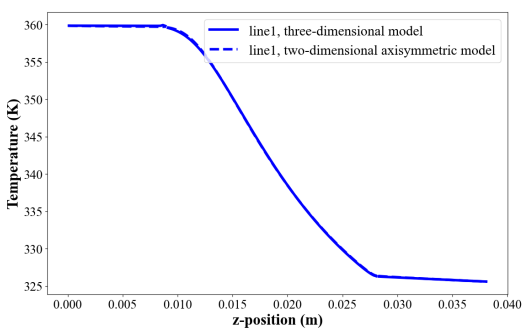

(a) Temperature fields (K) in the line1, plotting along the z-direction

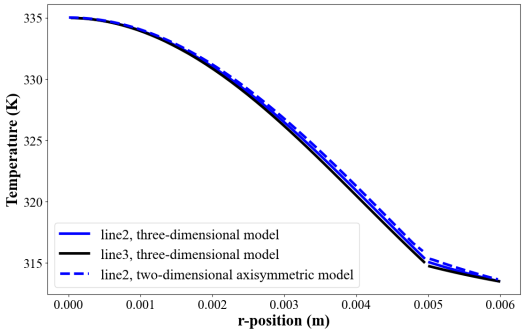

(b) Temperature fields (K) in the line2, line3, plotting along the r-direction

Figure 19: Temperature fields (K) comparison between the three-dimensional and two-dimensional axisymmetric numerical model

IP direction in this section. The different regions are identified as follows: flow1 (upwind flow field), sample (porous sample), flow2 (downwind flow field), and tube (quartz tube). The temperature fields (K) in the three-dimensional and two-dimensional axisymmetric numerical model at 100 s are shown in Fig.18, where Fig.18 (a) shows the temperature fields (K) in the yz plane (x=0 m) and xy plane (z=0.021 m) in the three-dimensional model, Fig.18 (b) shows it in the two-dimensional axisymmetric model. The flow direction is IP and the mass-flow rate is $7.68{\times}10^{-5} kg/s$. The LTE model (Eq.1) was considered for energy, mass and momentum conservation. The detailed expressions of the boundary conditions and of the initial conditions for the system of Eq.1 (LTE model) are provided in Table 4. The mesh refinement and time steps for the three-dimensional model are the same as the two-dimensional axisymmetric model mentioned in Appendix B. For the value of $c1$ and $c2$, the optimal results obtained in section 4.2 are used, that is, $c1 = 1.0$, $c2 = 1.98$. To analyze further the temperature difference between the three-dimensional and two-dimensional axisymmetric numerical model, we plot the temperature field in three lines, that is, line1 (in the yz plane and along the z-direction, the coordinates of the starting point are (0, 0, 0)), line2 (in the xy plane and along the y-direction, the coordinates of the starting point are (0, 0, 0.021)), line3 (in the xy plane and along the x-direction, perpendicular to line2.) The positions of line1, line2, and line3 are shown in Fig.18. As shown in Fig.19, the maximum temperature difference between the three-dimensional and two-dimensional axisymmetric simulations on line1 is 0.1 K, and on line2 is 0.3 K. For line 2 and line 3 in the three-dimensional simulation, the maximum temperature difference between them is 0.3 K. We can assume that the numerical results of the three-dimensional and two-dimensional axisymmetric models agree well on line 2 where the thermocouples are placed. This verifies that the two-dimensional axisymmetric model is suitable for this study, even when the flow direction is IP.

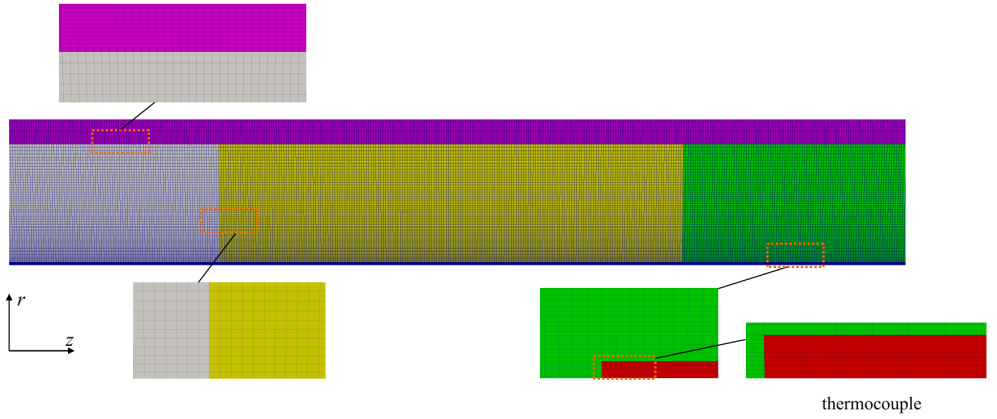

Figure 20: Mesh of the test section

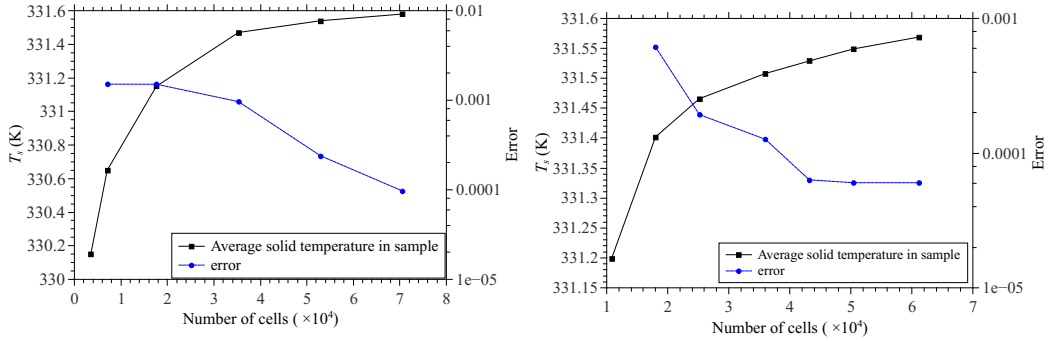

(a) flow direction (b) radial direction

Figure 21: Mesh dependency test in gas flow direction and radial direction

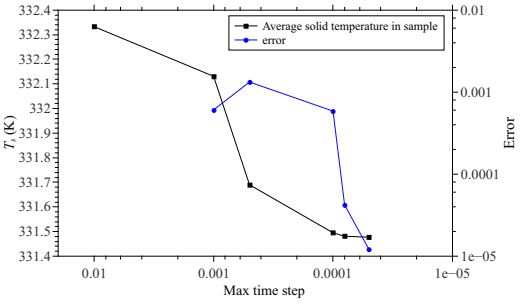

Figure 22: Time step dependency test

B. Appendix. Mesh and time convergence

A structured mesh was generated using the blockMesh application of OpenFoam. The mesh was refined at the near-wall and near-thermocouple regions. The final mesh is shown in Fig.20.

Mesh dependency was tested in flow and radial directions for the conditions presented in subsection 4.1. The mesh sensitivity analysis is plotted in Fig.21. While time-step independence is shown in Fig 22. As can be seen from Fig.21, when the number of cells increases in the gas flow direction from 5.29 $\times 10^4$ to 6.97 $\times 10^4$ and in the radial direction from 4.32$\times 10^4$ to 5.02 $\times 10^4$, there is no noticeable variation in the value of the volume averaged solid temperature T_s in the porous sample. Therefore, 5.29 $\times 10^4$ cells in the gas flow direction and 4.32 $\times 10^4$ cells in

the radial direction are acceptable for the numerical simulations. Adjustable time steps with a user-set maximum value are used in the simulations. When the maximum time step decreases from 1×10^{-4} s to 8×10^{-5} s, there is no noticeable evolution in the value of volume averaged solid temperature T_s. Therefore, the maximum time step is set to 1×10^{-4} s. The error in Fig.21 and Fig.22 are defined as:

$$\text{Error} = \left| \frac{T_{s,n+1} - T_{s,n}}{T_{s,n+1}} \right| \tag{12}$$

where the index n+1 indicates the numerical simulation with more mesh refinement and a smaller max time step respectively.

References

[1] H. K. Tran, C. E. Johnson, D. J. Rasky, F. C. L. Hui, M.-T. Hsu, T. Chen, Y. K. Chen, D. Paragas, L. Kobayashi, Phenolic impregnated carbon ablators (PICA) as thermal protection systems for discovery missions, NASA Technical Memorandum 110440 (1997) 1–70.

[2] M. Stackpoole, S. Sepka, I. Cozmuta, D. Kontinos, Post-flight evaluation of stardust sample return capsule forebody heatshield material, 46th AIAA Aerospace Sciences Meeting and Exhibit (2008). doi:10.2514/6.2008-1202.

[3] J. Lachaud, I. Cozmuta, N. N. Mansour, Multiscale approach to ablation modeling of phenolic impregnated carbon ablators, J. of Spacecr. and Rockets 47 (6) (2010) 910 – 921. doi:10.2514/1.42681.

[4] K. T. Edquist, B. R. Hollis, C. O. Johnston, D. Bose, T. R. White, M. Mahzari, Mars science laboratory heat shield aerothermodynamics: Design and reconstruction, J. of Spacecr. and Rockets 51 (4) (2014) 1106 – 1124. doi:10.2514/1.A32749.

[5] J. B. Meurisse, J. Lachaud, F. Panerai, C. Tang, N. N. Mansour, Multidimensional material response simulations of a full-scale tiled ablative heatshield, Aerosp. Sci. and Technol. 76 (2018) 497–511. doi:https://doi.org/10.1016/j.ast.2018.01.013.

[6] M. Mahzari, R. Beck, H. Hwang, J. Monk, J. Morgan, J. Williams, K. T. Edquist, Development and Sizing of the Mars2020 Thermal Protection System, 2022, p. 3951. doi:10.2514/6.2022-3951.

[7] J. B. Meurisse, G. B. Chatzigeorgis, P. V. Diaz, B. K. Bessire, F. Panerai, N. N. Mansour, Equilibrium model for the ablation response of silicone-coated pica, Int. J. of Heat and Mass Transf. 201 (2023). doi:10.1016/j.ijheatmasstransfer.2022.123523.

[8] M. Stackpoole, D. Kao, V. Qu, G. Gonzales, Post-flight evaluation of PICA and PICA-X : Comparisons of the stardust SRC and Space-X Dragon 1 forebody heatshield materials, 10th International Planetary Probe Workshop (IPPW-10) June 17-21 (2013).

[9] J. Bouilly, C. Plaindoux, Asterm: Maturation of a new low density ablative material, in: 7th European Workshop on TPS & Hot Structures, ESA/ESTEC, 2013, pp. 8–10.

[10] K. Triantou, K. Mergia, S. Florez, B. Perez, J. Barcena, W. Rotärmel, G. Pinaud, W. Fischer, Thermo-mechanical performance of an ablative/ceramic composite hybrid thermal protection structure for re-entry applications, Composites Part B: Engineering 82 (2015) 159 – 165. doi:10.1016/j.compositesb.2015.07.020.

[11] R. Jambunathan, D. A. Levin, A. Borner, J. C. Ferguson, F. Panerai, Prediction of gas transport properties through fibrous carbon preform microstructures using direct simulation monte carlo, Int. J. of Heat and Mass Transf. 130 (2019) 923 – 937. doi:10.1016/j.ijheatmasstransfer.2018.11.006.

[12] F. Panerai, J. D. White, T. J. Cochell, O. M. Schroeder, N. N. Mansour, M. J. Wright, A. Martin, Experimental measurements of the permeability of fibrous carbon at high-temperature, Int. J. of Heat and Mass Transf. 101 (2016) 267 – 273. doi:10.1016/j.ijheatmasstransfer.2016.05.016.

[13] J. Lachaud, N. N. Mansour, Porous-material analysis toolbox based on openfoam and applications, J. Thermophys Heat Transfer 28 (2) (2014) 191 – 202. doi:10.2514/1.T4262.

[14] E. Bartlett, R. Kendall, C. Moyer, R. Rindal, An analysis of the coupled chemically reacting boundary layer and charring ablator, part 1 summary report, NASA CR 1060 (1968) 1–96.

[15] C. B. Moyer, R. A. Rindal, An analysis of the coupled chemically reacting boundary layer and charring ablator. part 2-finite difference solution for the in-depth response of charring materials considering surface chemical and energy balances, NASA CR 1061 (1968) 1–168.

[16] J. Lachaud, T. Magin, I. Cozmuta, N. N. Mansour, A short review of ablative material response models and simulation tools, in: L. Ouwehand (Ed.), Proceedings of the 7th European Symposium on Aerothermodynamics, ESA SP-692, ISBN: 978-92-9221-256-8, no. 91, ESA, Noordwijk, The Netherlands, 2011, pp. 1–8.

[17] M. J. Wright, R. A. S. Beck, K. T. Edquist, D. Driver, S. A. Sepka, E. M. Slimko, W. H. Willcockson, Sizing and margins assessment of mars science laboratory aeroshell thermal protection system, J. of Spacecr. and Rockets 51 (4) (2014) 1125 – 1138. doi:10.2514/1.A32579.

[18] M. Wright, M. F. Hughes, M. Barnhardt, A. M. Calomino, An overview of technology investments in the nasa entry systems modeling project, 53rd AIAA Aerospace Sciences Meeting 1892 (2015) 1–40. doi:10.2514/6.2015-1892.

[19] J. Lachaud, J. B. Scoggins, T. E. Magin, M. G. Meyer, N. N. Mansour, A generic local thermal equilibrium model for porous reactive materials submitted to high temperatures, Int. J. of Heat and Mass Transf. 108 (2017) 1406–1417. doi:10.1016/j.ijheatmasstransfer.2016.11.067.

[20] F. Li, X. Huang, Y. Li, L. Lu, X. Meng, X. Yang, B. Sundén, Application and analysis of flip mechanism in the melting process of a triplex-tube latent heat energy storage unit, Energy Rep. 9 (2023) 3989–4004. doi:https://doi.org/10.1016/j.egyr.2023.03.037.

[21] H. Xu, L. Gong, C. Zhao, Y. Yang, Z. Xu, Analytical considerations of local thermal non-equilibrium conditions for thermal transport in metal foams, Int. J. Therm. Sci. 95 (2015) 73 – 87. doi:10.1016/j.ijthermalsci.2015.04.007.

[22] S. Chikh, A. Boumedien, K. Bouhadef, G. Lauriat, Analytical solution of non-darcian forced convection in an annular duct partially filled with a porous medium, Int. J. of Heat and Mass Transf. 38 (9) (1995) 1543–1551. doi:https://doi.org/10.1016/0017-9310(94)00295-7.

[23] A. D. Shugard, D. B. Robinson, A simple model of gas flow in a porous powder compact, Tech. rep. (4 2014). doi:10.2172/1127097.

[24] W. Lu, C. Zhao, S. Tassou, Thermal analysis on metal-foam filled heat exchangers. part i: Metal-foam filled pipes, Int. J. of Heat and Mass Transf. 49 (15) (2006) 2751–2761. doi:https://doi.org/10.1016/j.ijheatmasstransfer.2005.12.012.

[25] Z. Du, G. Liu, X. Huang, T. Xiao, X. Yang, Y.-L. He, Numerical studies on a fin-foam composite structure towards improving melting phase change, Int. J. Heat Mass Transf. 208 (2023) 124076. doi:https://doi.org/10.1016/j.ijheatmasstransfer.2023.124076.

[26] J. Florio Jr., J. B. Henderson, F. L. Test, R. Hariharan, A study of the effects of the assumption of local-thermal equilibrium on the overall thermally-induced response of a decomposing, glass-filled polymer composite, Int. J. of Heat and Mass Transf. 34 (1) (1991) 135 – 147. doi:10.1016/0017-9310(91)90181-D.

[27] N. Puiroux, M. Prat, M. Quintard, Non-equilibrium theories for macroscale heat transfer: ablative composite layer systems, Int. J. Therm. Sci. 43 (6) (2004) 541–554. doi:https://doi.org/10.1016/j.ijthermalsci.2003.11.004.

[28] N. Puiroux, M. Prat, M. Quintard, F. Laturelle, Macro-scale non-equilibrium heat transfer in ablative layer composite layers, in: 8th AIAA/ASME Joint Thermophysics and Heat Transfer Conference, 2003, p. 3336. doi:https://doi.org/10.2514/6.2002-3336.

[29] J. Scoggins, H. Hassan, Pyrolysis mechanism of pica, in: 10th AIAA/ASME Joint Thermophysics and Heat Transfer Conference, 2010, p. 4655. doi:10.2514/6.2010-4655.

[30] M. Kaviany, Principles of heat transfer in porous media, Springer Science & Business Media, 2012.

[31] H. Scandelli, A. Ahmadi-Senichault, C. Levet, J. Lachaud, Computation of the permeability tensor of non-periodic anisotropic porous media from 3d images, Transp. Porous Media 142 (3) (2022) 669 – 697. doi:10.1007/s11242-022-01766-8.

[32] N. Zamel, X. Li, J. Shen, J. Becker, A. Wiegmann, Estimating effective thermal conductivity in carbon paper diffusion media, Chem. Eng. Sci. 65 (13) (2010) 3994–4006. doi:https://doi.org/10.1016/j.ces.2010.03.047.

[33] I. Tavman, Effective thermal conductivity of granular porous materials, Int. Commun. Heat Mass Transfer 23 (2) (1996) 169–176. doi:https://doi.org/10.1016/0735-1933(96)00003-6.

[34] Z. Abdulagatova, I. Abdulagatov, V. Emirov, Effect of temperature and pressure on the thermal conductivity of sandstone, Int. J. Rock Mech. Min. Sci. 46 (6) (2009) 1055–1071. doi:https://doi.org/10.1016/j.ijrmms.2009.04.011.

[35] M. Quintard, M. Kaviany, S. Whitaker, Two-medium treatment of heat transfer in porous media: numerical results for effective properties, Adv. Water Resour. 20 (2) (1997) 77–94. doi:https://doi.org/10.1016/S0309-1708(96)00024-3.

[36] M. Quintard, S. Whitaker, One- and two-equation models for transient diffusion processes in two-phase systems, Vol. 23, 1993, pp. 369–464. doi:https://doi.org/10.1016/S0065-2717(08)70009-1.

[37] K.-T. Hsiao, S. G. Advani, Modified effective thermal conductivity due to heat dispersion in fibrous porous media, Int. J. of Heat and Mass Transf. 42 (7) (1999) 1237–1254. doi:https://doi.org/10.1016/S0017-9310(98)00246-4.

[38] M. Quintard, Introduction to heat and mass transport in porous media, Porous Media Interaction with High Temperature and High Speed Flows, Von Karman Institude for Fluid Dynamics, Rhode Saint Genese, Belgium (2015).

[39] J. Chevalier, J. Lachaud, On the effect of the internal gas flow velocity on the thermal conductivity of porous thermal protection systems, in: 2nd International Conference on Flight Vehicles, Aerothermodynamics and Re-entry Missions and Engineering, 2022.

[40] X. lin Xia, X. Chen, C. Sun, Z. huan Li, B. Liu, Experiment on the convective heat transfer from airflow to skeleton in open-cell porous foams, Int. J. of Heat and Mass Transf. 106 (2017) 83–90. doi:https://doi.org/10.1016/j.ijheatmasstransfer.2016.10.053.

[41] G. Gürüf, İsmail Solmuş, K. Bilen, Özgür Bayer, Experimental based numerical approach for determination of volumetric heat transfer coefficients of modified graphite foams, Appl. Therm. Eng. 174 (2020) 115310. doi:https://doi.org/10.1016/j.applthermaleng.2020.115310.

[42] J.-J. Hwang, G.-J. Hwang, R.-H. Yeh, C.-H. Chao, Measurement of Interstitial Convective Heat Transfer and Frictional Drag for Flow Across Metal Foams , J. of Heat Transfer 124 (1) (2001) 120–129. doi:10.1115/1.1416690.

[43] C. T. DeGroot, A. G. Straatman, Closure of non-equilibrium volume-averaged energy equations in high-conductivity porous media, Int. J. of Heat and Mass Transf. 54 (23) (2011) 5039–5048. doi:https://doi.org/10.1016/j.ijheatmasstransfer.2011.07.018.

[44] F. Kuwahara, M. Shirota, A. Nakayama, A numerical study of interfacial convective heat transfer coefficient in two-energy equation model for convection in porous media, Int. J. of Heat and Mass Transf. 44 (6) (2001) 1153–1159. doi:https://doi.org/10.1016/S0017-9310(00)00166-6.

[45] F. E. Teruel, Entrance effect on the interfacial heat transfer and the thermal dispersion in laminar flows through porous media, Int. J. Therm. Sci. 104 (2016) 172–185. doi:https://doi.org/10.1016/j.ijthermalsci.2016.01.005.

[46] A. Nakayama, A note on the confusion associated with the interfacial heat transfer coefficient for forced convection in porous media, Int. J. of Heat and Mass Transf. 79 (2014) 1–2. doi:https://doi.org/10.1016/j.ijheatmasstransfer.2014.07.088.

[47] F. E. Teruel, L. Díaz, Calculation of the interfacial heat transfer coefficient in porous media employing numerical simulations, Int. J. of Heat and Mass Transf. 60 (2013) 406–412. doi:https://doi.org/10.1016/j.ijheatmasstransfer.2012.12.022.

[48] Z. Wu, C. Caliot, G. Flamant, Z. Wang, Numerical simulation of convective heat transfer between air flow and ceramic foams to optimise volumetric solar air receiver performances, Int. J. of Heat and Mass Transf. 54 (7) (2011) 1527–1537. doi:https://doi.org/10.1016/j.ijheatmasstransfer.2010.11.037.

[49] J. Petrasch, F. Meier, H. Friess, A. Steinfeld, Tomography based determination of permeability, dupuit–forchheimer coefficient, and interfacial heat transfer coefficient in reticulate porous ceramics, Int. J. Heat Fluid Flow 29 (1) (2008) 315–326. doi:https://doi.org/10.1016/j.ijheatfluidflow.2007.09.001.

[50] H. Scandelli, A. Ahmadi-Senichault, S. Liu, J. Lachaud, Volumetric heat transfer coefficient: Numerical evaluation and introductory analysis to anisotropic effect, to appear (2022).

[51] R. V. X.Fu, J. Gore, Measurement and correlation of volumetric heat transfer coefficients of cellular ceramics, Exp. Therm Fluid Sci. 17 (4) (1998) 285–293. doi:https://doi.org/10.1016/S0894-1777(98)10002-X.

[52] K. Ando, H. Hirai, Y. Sano, An accurate experimental determination of interstitial heat transfer coefficients of ceramic foams using the single blow method, The Open Transport Phenomena Journal 5 (1) (2013). doi:10.2174/1877729501305010007.

[53] T. Xiao, G. Liu, J. Guo, G. Shu, L. Lu, X. Yang, Effect of metal foam on improving solid–liquid phase change in a multi-channel thermal storage tank, Sustain. Energy Technol. Assess. 53 (2022) 102533. doi:https://doi.org/10.1016/j.seta.2022.102533.

[54] N. Wakao, S. Kaguei, T. Funazkri, Effect of fluid dispersion coefficients on particle-to-fluid heat transfer coefficients in packed beds: Correlation of nusselt numbers, Chem. Eng. Sci. 34 (3) (1979) 325–336. doi:https://doi.org/10.1016/0009-2509(79)85064-2.

[55] L. Younis, R. Viskanta, Experimental determination of the volumetric heat transfer coefficient between stream of air and ceramic foam, Int. J. of Heat and Mass Transf. 36 (6) (1993) 1425–1434. doi:https://doi.org/10.1016/S0017-9310(05)

80053-5.

[56] K. Kamiuto, S. S. Yee, Heat transfer correlations for open-cellular porous materials, Int. Commun. Heat Mass Transfer 32 (7) (2005) 947–953. doi:https://doi.org/10.1016/j.icheatmasstransfer.2004.10.027.

[57] A. J. Fuller, T. Kim, H. P. Hodson, T. J. Lu, Measurement and interpretation of the heat transfer coefficients of metal foams, Proceedings of the Institution of Mechanical Engineers, Part C: J. Mech. Eng. Sci 219 (2) (2005) 183–191. doi:10.1243/095440605X8414.

[58] G. Liu, Z. Du, T. Xiao, J. Guo, L. Lu, X. Yang, K. Hooman, Design and assessments on a hybrid pin fin-metal foam structure towards enhancing melting heat transfer: An experimental study, Int. J. Therm. Sci. 182 (2022) 107809. doi:https://doi.org/10.1016/j.ijthermalsci.2022.107809.

[59] P. Renze, K. Akermann, Simulation of conjugate heat transfer in thermal processes with open source cfd, ChemEngineering 3 (2) (2019) 59. doi:https://doi.org/10.3390/chemengineering3020059.

[60] S. E. Gustafsson, Transient plane source techniques for thermal conductivity and thermal diffusivity measurements of solid materials, Rev. Sci. Instrum. 62 (3) (1991) 797–804. doi:10.1063/1.1142087.

[61] F. Panerai, J. C. Ferguson, J. Lachaud, A. Martin, M. J. Gasch, N. N. Mansour, Micro-tomography based analysis of thermal conductivity, diffusivity and oxidation behavior of rigid and flexible fibrous insulators, Int. J. of Heat and Mass Transf. 108 (2017) 801–811. doi:https://doi.org/10.1016/j.ijheatmasstransfer.2016.12.048.

[62] K. Stephan, R. Krauss, A. Laesecke, Viscosity and thermal conductivity of nitrogen for a wide range of fluid states, J. Phys. Chem. Ref. Data 16 (4) (1987) 993–1023. doi:10.1063/1.555798.

[63] F. Torres-Herrador, A. Turchi, K. M. Van Geem, J. Blondeau, T. E. Magin, Determination of heat capacity of carbon composites with application to carbon/phenolic ablators up to high temperatures, Aerosp. Sci. and Technol. 108 (2021) 106375. doi:https://doi.org/10.1016/j.ast.2020.106375.

[64] T. Esence, A. Bruch, S. Molina, B. Stutz, J.-F. Fourmigué, A review on experience feedback and numerical modeling of packed-bed thermal energy storage systems, Sol. Energyy 153 (2017) 628–654. doi:https://doi.org/10.1016/j.solener.2017.03.032.

[65] B. M. Adams, W. J. Bohnhoff, M. S. Dalbey, K.R.and Ebeida, J. P. Eddy, M. S. Eldred, R. W. Hooper, P. D. Hough, K. T. Hu, J. D. Jakeman, M. Khalil, K. A. Maupin, J. A. Monschke, E. M. Ridgway, A. A. Rushdi, D. T. Seidl, J. A. Stephens, L. P. Swiler, J. G. Winokur, Dakota, a multilevel parallel object-oriented framework for design optimization, parameter estimation, uncertainty quantification, and sensitivity analysis: Version 6.15 user's manual, Sandia Technical Report SAND2020-12495 (2021).

[66] J. Gablonsky, Direct version 2.0 userguide technical report, CRSC-TR01-08, Center for Research in Scientific Computation (2001).

[67] J. E. Dennis Jr, D. M. Gay, R. E. Walsh, An adaptive nonlinear least-squares algorithm, ACM Trans. Math. Software 7 (3) (1981) 348–368.

[68] H. Scandelli, A. Ahmadi-Senichault, J. Lachaud, Two-temperature ablative material response model with application to stardust and msl atmospheric entries, Aerospace Science and Technology 137 (2023) 108297. doi:https://doi.org/10.1016/j.ast.2023.108297.